

# **Fabrication of biomedical cancellous NiTi by starch consolidation of pre-alloyed powder**

by

ROBIN BENGTSSON

**Diploma work No. 86/2012**

at Department of Materials and Manufacturing Technology  
CHALMERS UNIVERSITY OF TECHNOLOGY  
Gothenburg, Sweden

Diploma work in the Master Program Advanced Engineering Materials

**Performed at:** Chalmers University of Technology  
Department of Materials and Manufacturing Technology  
Chalmers University of Technology  
SE – 412 96 Gothenburg

**Supervisor:** Dr. Kumar Babu Surreddi  
Department of Materials and Manufacturing Technology  
Chalmers University of Technology  
SE – 412 96 Gothenburg

**Examiner:** Prof. Lars Nyborg  
Department of Materials and Manufacturing Technology  
Chalmers University of Technology  
SE – 412 96 Gothenburg

**Fabrication of biomedical cancellous NiTi by starch consolidation of pre-alloyed powder**  
ROBIN BENGTTSSON

© ROBIN BENGTTSSON, 2012.

Diploma work no 86/2012  
Department of Materials and Manufacturing Technology  
Chalmers University of Technology  
SE-412 96 Gothenburg  
Sweden  
Telephone + 46 (0)31-772 1000

Till Mamma och Pappa



## **SAMMANFATTNING**

Minnesmetaller är legeringar som genom fastransformation och/eller deformation har superelastiska egenskaper och minnes-egenskaper. Det förstnämnda innebär inte någon temperaturändring utan sker spontant vid spänningsavtagande. Det andra innebär att återhämta mycket stora formförändringar genom upphettning.

NiTi är en minnesmetall bestående av lika antal nickel- som titan-atomer. De ovanstående egenskaperna ihop med den bevisade biokompatibiliteten och dess likhet med motsvarande egenskaper hos ben gör NiTi till ett fullgott alternativ till redan etablerade biomaterial som rostfritt stål och titan.

På grund av den relativt höga smälttemperaturen hos NiTi är pulvermetallurgi (PM) en viktig tillverkningsteknik, där smälttemperaturen inte önskas varken nås eller passeras. Bulk-NiTi tillverkas idag för till exempel guidewires och rörtätningar. Emellertid utökar tillverkning av porös NiTi användningsområdet med till exempel filterinsatser och ersättning av spongiöst ben. Med hjälp av PM kan detta åstadkommas. En tillverkningsmetod kallas stärkelsekonsolidering, och efterföljs av fastfas-sintring. Metoden innefattar stärkelse vilket används som både bindemedel (konsolideringsmedel) och porformare. Med legerat NiTi-pulver så utvärderas i detta examensarbete denna metod ihop med simpel pulver-sintring genom mekaniska tester och mikrostrukturanalys. Resultaten visar att det är möjligt att tillverka porösa strukturer av NiTi för utveckling av önskade superelastiska egenskaper.

Fabrication of biomedical cancellous NiTi by starch consolidation of pre-alloyed powder  
ROBIN BENGTTSSON  
Department of Materials and Manufacturing Technology  
Chalmers University of Technology

## **ABSTRACT**

Shape memory alloys are alloys that through phase change and/or deformation have the properties of superelasticity and shape memory effect (SME). The first implies no temperature change and occurs upon stress release. The second implies recovering very large shape changes through heating.

NiTi is a shape memory alloy of equiatomic configuration. Proven biocompatibility and above mentioned properties with their similarity to corresponding properties of bone makes it an alternative very comparable to already established implant materials such as stainless steel and titanium.

Due to the relatively high melting temperature of NiTi, powder metallurgy is a key fabrication technology, where passing or reaching melting temperature is avoided. Today bulk NiTi is made for e.g. guide-wires and pipe seals. However, fabricating NiTi in a porous form expands the application area with e.g. filter inserts and cancellous bone replacements. With the use of powder metallurgy this can be achieved. One fabrication method is starch consolidation followed by solid state sintering. It implies using starch as both binder and pore former. With pre-alloyed NiTi powder, this method and loose powder sintering are evaluated by mechanical tests and analysis of microstructure in this thesis. The results show that it is possible to generate porous NiTi structures for further development of desired superelastic behaviour.

Keywords: NiTi, PM, porous, pre-alloyed powder, starch consolidation.

# TABLE OF CONTENTS

1. INTRODUCTION.....	1
1.1 Background .....	1
1.2 Aim and goal .....	1
1.3 Delimitations .....	1
2. THEORY.....	3
2.1 Shape memory alloys .....	3
2.2 NiTi .....	3
2.2.1 Physical metallurgy .....	3
2.2.2 Shape memory effect and superelasticity .....	4
2.2.3 Mechanical properties .....	7
2.2.4 Applications.....	9
2.3 Powder metallurgy .....	10
2.3.1 General principles of powder metallurgy .....	10
2.3.2 NiTi in powder metallurgy .....	11
2.4 Starch consolidation .....	11
3. METHODOLOGY.....	13
3.1 Powder.....	13
3.2 Sintering .....	13
3.2.1 Loose powder sintering .....	13
3.2.2 Starch consolidation and sintering.....	14
3.3 X-ray diffraction.....	16
3.4 Scanning electron microscopy.....	16
3.5 Electrical discharge machining.....	17
3.6 Porosity measurements.....	17
3.6.1 Powder.....	17
3.6.2 Sintered samples.....	17
3.7 Microhardness .....	17
3.8 Mechanical testing.....	18
4. RESULTS.....	19
4.1 Sample production.....	19
4.1.1 Appearance of loose powder sintered samples.....	19
4.1.2 Appearance of starch consolidated samples .....	20
4.2 Geometrical and Porosity measurements .....	20
4.3 Microhardness .....	20
4.4 SEM and EDX.....	21
4.4.1 SEM.....	21
4.4.2 EDX.....	30
4.5 XRD .....	33
4.6 Mechanical testing.....	34
4.6.1 As-sintered test pieces .....	34
4.6.2 Anisotropy .....	35
4.6.3 Heat-treated test pieces.....	36
4.6.4 Cyclic tests .....	37
5. DISCUSSION .....	39
5.1 Sample production.....	39
5.2 Microstructure .....	41
5.3 Porosity and shrinkage .....	42
5.4 Mechanical properties .....	43
5.5 Biocompatibility considerations.....	45

6. CONCLUSIONS.....	47
7. FUTURE WORK.....	49
8. REFERENCES.....	51
APPENDIX.....	55-59

## DEFINITIONS

$A_f$	Temperature at which transformation into austenite finishes upon heating
$A_s$	Temperature at which transformation into austenite starts upon heating
B2	Crystal structure of simple cubic phase, also called CsCl structure
B19'	Crystal structure of monoclinic phase
$d_{50}$	A measure of particle size, the median size of the powder particle distribution
DCT	Direct-Consolidation Technique, a powder shaping technique group
EDM	Electrical Discharge Machining
EDX	Energy Dispersive X-ray spectroscopy
$e_f$	Engineering strain at fracture
EHT	Electron High Tension
HV	Hardness Vickers
$M_f$	Temperature at which transformation into martensite finishes upon cooling
$M_s$	Temperature at which transformation into martensite starts upon cooling
Ni	Nickel
PDF	Powder Diffraction File (XRD data file)
R3	Crystal structure of rhombohedral phase
$R_f$	Temperature at which transformation into R-phase finishes
$R_s$	Temperature at which transformation into R-phase starts
R-phase	Tetragonal martensite phase of NiTi
SEM	Scanning Electron Microscopy
$s_f$	Engineering stress at fracture
SMA	Shape Memory Alloy
SME	Shape Memory Effect
$s_u$	Engineering ultimate tensile strength
$s_y$	Engineering yield strength
$t$	Time
$T$	Temperature
Ti	Titanium
XRD	X-Ray Diffraction



# 1. INTRODUCTION

This chapter aims to introduce the background to this thesis, and also its aim and delimitations.

## 1.1 Background

Generally, shape memory alloys can show two interesting kinds of behaviour:

- Shape memory
- Superelasticity (strain induced due to loading can be recovered during unloading)

These properties together with biocompatibility have made NiTi an excellent alternative for bone implants as compared to conventional stainless steel and titanium (Thierry et al., 2002, Gil & Planell, 2000, Ryhanen et al., 1998). Manufacturing of such biomedical components by means of powder metallurgy (PM) is a good solution to obtain near net-shape components with very little material wastage (Sanderow, 1998). In addition, a porous structure enables ingrowth of new bone and tissues into the implants. However, it is difficult to produce porous shape memory alloy (SMA) products through conventional sintering methods (Bansiddhi et al., 2008). In this thesis, a new forming method called “starch consolidation” is explored to fabricate desired sintered products for biomedical parts such as porous bone implants. Other applications could be filters where the shape memory effect can be used to change the flow.

Other than the sustainability gain from low energy use and material wastage of PM (Sanderow, 1998), the use of starch is a sustainable choice. The starch used in this experimental work is naturally generated inside and extracted from potatoes, showing no toxicity or irritability to living organisms during pre-use, in-use or post-use.

## 1.2 Aim and goal

The aim of this thesis is to evaluate the possibilities to manufacture porous NiTi SMA components for biomedical applications by using starch consolidation followed by sintering using pre-alloyed NiTi powder. The porosity measurements are performed from the geometry and weight of the sintered samples. The mechanical properties are obtained from the compression testing and microhardness tests. The structural information is obtained from the X-ray diffraction (XRD) analysis and the microstructure and the composition of different phases are obtained from the scanning electron microscopy (SEM) and energy-dispersive X-ray spectroscopy (EDX). The goal is to produce bulk porous samples by i) loose powder sintering and by ii) starch consolidation with subsequent sintering using pre-alloyed NiTi powder. Having pre-alloyed NiTi powder instead of a mix of nickel and titanium powders means increased chance of homogeneous microstructure, which is crucial for the material properties. The bulk samples are produced to make it possible to perform the above mentioned tests in full extent. Also, the goal is to show advantages and drawbacks of the fabrication methods and to generate usable experience for future work.

## 1.3 Delimitations

Complete evaluation of the fabrication methods is not reasonable to aim for within the format of this master thesis study. Therefore certain limitations have been set as follows:

- The work does not include any major developments of the starch consolidation method itself, neither regarding processing aids, materials use or process parameters.
- The thermal characterization and sintering kinetics of the material will not be evaluated in detail.

- The biocompatibility of the sintered samples will not be evaluated and conclusions regarding this will be based solely on work done by other researchers.
- Major heat treatments of powder and sintered products will not be performed.
- Mechanical testing at different temperatures will not be covered in this work.

## 2. THEORY

This chapter aims to cover the theory needed to grasp the contents of this thesis.

### 2.1 Shape memory alloys

The shape memory alloys (SMA) are alloys that by deforming at low temperature in a martensitic state can be transformed into the parent phase upon heating (Wayman, 1993). This transformation back gives the alloy a sense of having a memory. The micromechanics behind this are more thoroughly described in subchapter 2.2.2. Many materials can establish some level of memory effect but very few alloy systems (about 20) exhibit perfect and 100% shape recovery, they are Ag-Cd, Au-Cd, Cu-Zn, Cu-Zn-Si, Cu-Zn-Sn, Cu-Zn-Al, Cu-Zn-Ga, Cu-Al-Ni, Cu-Sn, Cu-Sn, Cu-Au-Zn, Ni-Al, Ti-Ni, Ti-Ni-Cu, Ti-Pd-Ni, In-Ti, In-Cd and Mn-Cd (Otsuka & Wayman, 1998).

### 2.2 NiTi

This subchapter presents the features and use of the intermetallic NiTi phase in this thesis study. A broad perspective of the NiTi is not in the scope of this thesis. Therefore, this chapter is only within the scope of science used in this thesis. Please see references following for further reading.

#### 2.2.1 Physical metallurgy

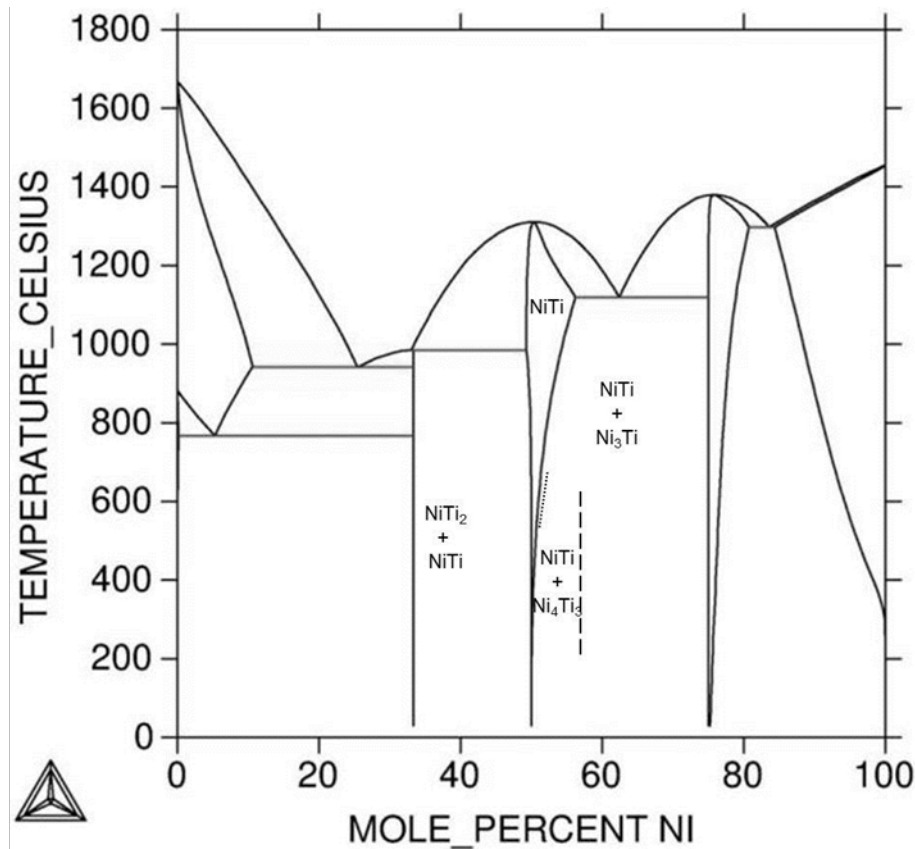


**Figure 1:** Ti-Ni phase diagram of temperature vs mole percent Ni (Bellen et al., 2010) modified with  $\text{Ni}_4\text{Ti}_3$  line (dashed) and formation line of this intermetallic upon ageing (dotted) (Otsuka & Kakeshita, 2002).

The phase diagram of Ti-Ni derived from Thermo-Calc calculations is shown in Figure 1. The area of the intermetallic NiTi starts at its melting temperature at around 1300°C and widens to reach its maximum width at around 1120°C to then continue to thin out as temperature decreases. The titanium rich (left) intermetallic phase boundary side is nearly vertical suggesting an absence of major effects from prior thermal history in the titanium composition. The nickel solubility however, increases

rapidly with temperature heading for the area's maximum width at about 1120°C. This feature suggests a precipitation hardening being present. The solubility of other phases in NiTi becomes negligible at about 500°C (Wasilevski et al., 1971).

The three phases  $\text{Ni}_4\text{Ti}_3$ ,  $\text{Ti}_2\text{Ni}_3$  and  $\text{TiNi}_3$  appear in this order during ageing for higher ageing temperature and longer time (Nishida et al., 1986). The first two were shown to occur as intermediate phase precipitates and the third is an equilibrium phase. The study of this ageing behaviour was done with Ni-48at.%Ti, the powder used in this thesis work is Ni-49at.%Ti. However, local differences in composition are possible and the above facts from Wasilevski et al. in 1971 are probable to be of use.

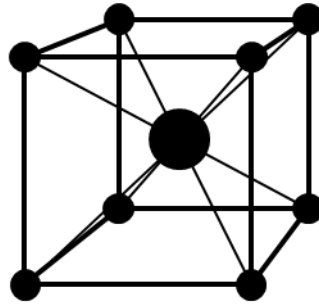


**Figure 2:** The B2 structure. In this example the smaller atoms form a simple cubic structure and encase the larger atom in the center.

At room temperature the NiTi phase has a B2 (similar to CsCl) structure with a lattice constant of 0.3015 nm, which is the side length of the unit cell, see Figure 2. This B2 structure is a simple cubic of one type of atom in each corner and the other type of atom in the centre of the cube. The B2 phase is retained when the intermetallic is quenched or slowly cooled to room temperature. This phase plays a key role in the martensitic transformation and the associated shape memory effect which is presented later in this subchapter.

Towards the titanium-richer area, the phase  $\text{Ti}_2\text{Ni}$  (see Fig. 1) is of cubic structure and has a unit cell containing 96 atoms and a lattice constant of 1.132 nm (Mueller & Knott, 1963). For NiTi, the most common oxide appearing is  $\text{Ti}_4\text{Ni}_2\text{O}$ , which has nearly the same structure as  $\text{Ti}_2\text{Ni}$ .

As stated above, the  $\text{Ni}_4\text{Ti}_3$  phase precipitates at lower ageing temperatures and less ageing times and forms in lenticular shape (Koskimaki et al., 1969). The phase is very important with respect to shape memory characteristics, which will be discussed later in this subchapter. The structure of this phase is R3 and has a rhombohedral unit cell with sides of  $a = 0.670$  nm and  $\alpha = 113.8^\circ$  (Saburi et al., 1986).

At higher ageing temperatures and longer ageing times than for the  $\text{Ni}_4\text{Ti}_3$  phase and at lower temperatures and shorter times than for the  $\text{TiNi}_3$ , the precipitate appearing is  $\text{Ti}_2\text{Ni}_3$  (Hara et al., 1997). This precipitate actually can occur in two different phases depending on temperature. The phase at higher temperatures has a tetragonal structure with lattice parameters of  $a = 0.3095$  nm and  $c = 1.3585$  nm (at 373 K). The lower temperature phase is of orthorhombic structure with  $a = 0.4398$  nm,  $b = 0.4370$  nm and  $c = 1.3544$  nm (at 298 K).

The  $\text{TiNi}_3$  phase appearing at the higher ageing temperatures and longer ageing times is of hexagonal structure. It has lattice constants  $a = 0.51010$  nm and  $c = 0.83067$  nm (Taylor & Floyd, 1950).

### 2.2.2 Shape memory effect and superelasticity

In order to explain shape memory effect (SME) and superelasticity, some additional information needs to be stated here. An alloy possessing these two phenomena has  $M_s$  and  $M_f$  temperatures at which it starts and finishes, respectively, transforming into martensite upon cooling, therefore  $M_s > M_f$ . The alloy

also has  $A_s$  and  $A_f$ , temperatures at which it starts and finishes respectively to retransform from martensite upon heating, therefore  $A_s < A_f$ , also  $A_s > M_s$ . Apart from temperature induced, the martensite can also be stress-induced which will be described below. The values of the critical transformation temperatures depend on the treatment history of the material, depicted by e.g. heat treatment, grain size, precipitation, etc.

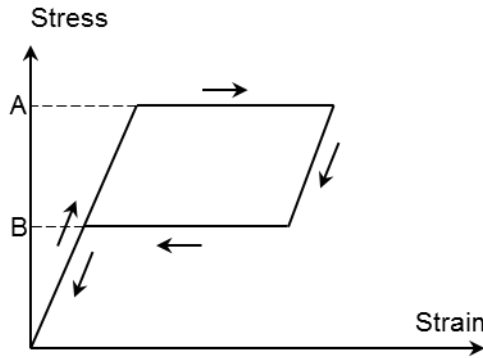


**Figure 3:** Stress-strain curve schematically illustrated at a temperature a little above  $A_f$  for Ti-50.6at.%Ni. The critical stress to induce martensite (A) and the reverse transformation (B) is marked. Maximum stress and strain are in the order of 200-250 MPa and 4-5% respectively (Miyazaki et al., 1981).

Figure 3 shows the schematic stress-strain curve of a Ti-50.6at.%Ni alloy tested at just above  $A_f$  (Miyazaki et al., 1981). The specimen was pre-test solution-treated at 1273 K for 1 h, followed by quenching in water. This treatment was done to form homogenous solid solution state parent phase. At temperatures below  $A_f$ , the recovery to previous strain at critical stress B does not occur, and at temperatures below  $M_s$ , the critical stress to reach A increases. At temperatures above  $A_f$ , the critical stress at A increases with temperature as does the gap between load and unloading line which is zero in the figure. The critical stresses for curves like this (i.e. A and B) can be plotted as a function of temperature, see Figure 4 below.

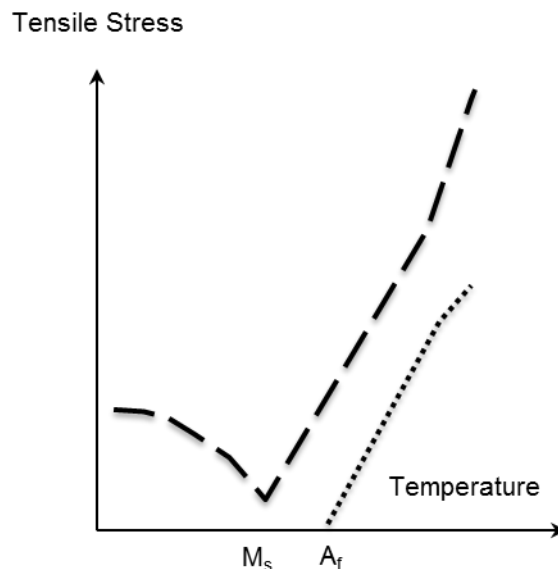


**Figure 4:** Schematic illustration of critical stresses as a function of temperature for inducing martensites ( $T > M_s$ ) and for yielding ( $T < M_s$ ) (dashed line) and for reverse transformation (dotted line) (Miyazaki et al., 1981).

The  $M_s$  of the figure was determined by electrical resistivity measurements (Miyazaki et al., 1981), and it correlates rather well with the minimum stress curve upon loading. Regarding the mechanical

behaviour below and above the minimum point, it corresponds to the deformation of martensite and to the stress-induced martensitic transformation respectively. From the figure, it can be stated that at temperatures a little above  $A_f$  (here 221 K) the plastic strain recovers during unloading and forms a closed loop, while at temperatures below  $A_f$  the strain remains upon unloading. This residual strain of the latter case can however be recovered by heating the specimen to temperatures above  $A_f$ , causing a transformation of martensite into the parent phase. The first case, not involving any change of temperature, is referred to as superelasticity, while the second case, involving a raise of temperature to recover, is referred to as shape memory effect.

Regarding SME, two cases are present depending on temperature (Otsuka et al., 1976). If the sample is fully martensitic, i.e. when the temperature is  $\leq M_f$ , the deformation is purely of the martensite. But if the temperature is  $>M_f$  or especially  $>M_s$ , the deformation is performed at least partially by the stress-induced martensitic formation, which is a similar case as for superelasticity, with the difference of martensite stability upon release of stress. The martensite remains (stable) upon stress release in the case of SME. The free energy difference between the parent phase and the martensite is the driving force for both SME and superelasticity.

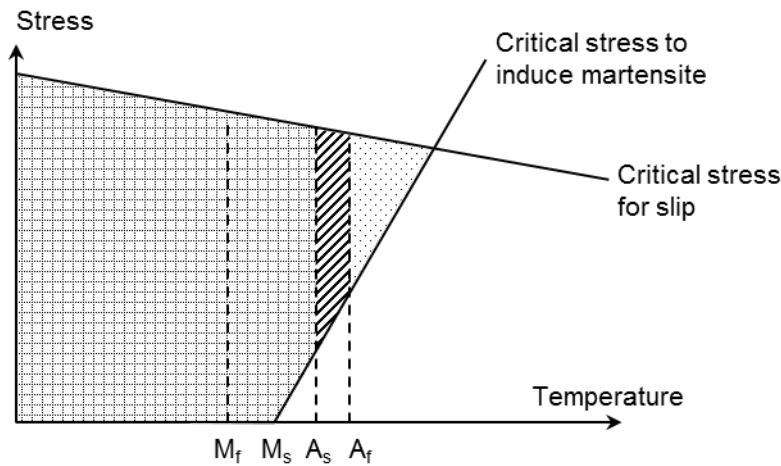


**Figure 5:** Schematic stress vs. temperature diagram to illustrate the pure shape memory effect area (squared), pure superelastic area (dotted) and combined area (striped) (Otsuka & Shimizu, 1986).

The possible presence of both SME and superelasticity is illustrated in Figure 5 above. Depending on the testing temperature, either SME or superelasticity or both effects occur as shown in the figure. In the figure, the slip line represents the critical stress for slip. For a situation where the critical stress for slip is much lower (lying much lower than in the figure), the irreversible process of slipping will occur. This will decrease or even eliminate the superelasticity. But for the situation seen in Figure 5, the possibilities of superelasticity are fair, because the martensitic deformation can then occur by twinning instead (see Fig. 6), which is reversible. In the case of Ti-50at.%Ni the SME and superelasticity is good only if proper heat treatment has been performed. In an ideal solution-treated condition, without any precipitation hardening to increase the critical slip stress, the slip is too easily introduced. Also as shown in the figure, a line from  $M_s$  is the critical stress to induce martensite, which extends towards higher stress and temperature since the transformation is a shear-like mechanism and therefore is assisted by the stress.

Regarding the more in detail description of the martensitic transformations there are two types. The first one is the change from the cubic B2 phase to the martensitic monoclinic B19' phase, a transformation typically realised within around 30°C hysteresis (Miyazaki & Otsuka, 1986). This

appears when measurements are made on binary Ni-Ti alloys quenched from high temperature B2 parent phase. The second type of martensitic transformation is characterized by a sharp increase in resistivity upon cooling referred to as the R-phase transformation (Miyazaki & Otsuka, 1984). This phase was first considered to be of rhombohedral, thereby the name. Further studies show that it is trigonal. This is a transformation typically realised within around 2°C hysteresis. This data was produced for Ti-47at.%Ni-3at.%Fe but the R-phase transformation is also available in binary Ti-Ni alloys, if properly cold-worked and annealed. Summarized we have two paths from B2 to B19', they are direct: B2 → B19'; and indirect: B2 → R → B19'. The R-phase transformation has finish and start temperatures referred to as  $R_f$  and  $R_s$ , respectively.

### 2.2.3 Mechanical properties

One of the biggest challenges dealing with the shape memory alloy family is developing the proper processing procedures to obtain the desired properties (Duerig & Pelton, 1994). Therefore any set values of NiTi properties are questionable to state. However, table 1, shows some of the ASM Handbook properties for the alloy in annealed condition. Notable is the fact that the values are for equiatomic alloy with an  $A_f$  of 110°C.

**Table 1:** Equiatomic NiTi property values, partially distinguishing between B2 phase (simple cubic) and B19' phase (martensite) (Duerig & Pelton, 1994).

Property		Property value
Melting temperature		1300°C
Density		6450 kg/m <sup>3</sup>
E-modulus	B2 phase	approx. 83 GPa
	B19' phase	approx. 28-41 GPa
Yield strength	B2 phase	195-690 MPa
	B19' phase	70-140 MPa
Ultimate tensile strength		895 MPa
Transformation temperatures		-200 to 110°C
Shape memory strain		8.5% maximum

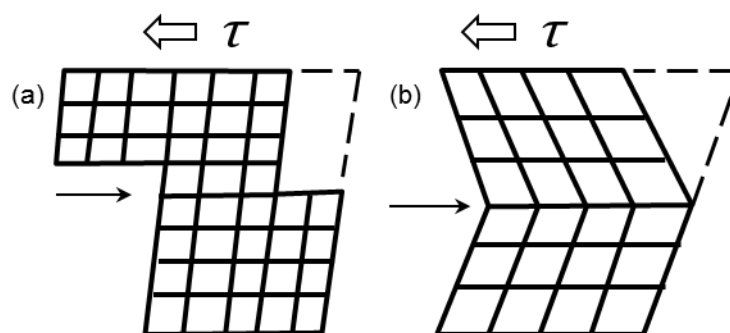


**Figure 6:** Schematic illustration of a) slip and, b) twinning in a crystal with their respective planes (thin arrow) and direction of shear stress ( $\tau$ ). At each line crossing an atom is situated. Dashed lines represent their previous shapes (Smallman & Ngan, 2007).

The important deformations at hand regarding NiTi is either slip or twinning, where the latter is the desired, since it is reversible (Smallman & Ngan, 2007). In the case of slipping, the top half of the crystal moves along certain slip planes on the bottom half, see Figure 6a. This is performed in such a way that the atoms move forward a whole number of lattice vectors thereby maintaining the continuity of the lattice. In the case of twinning the movement of the atoms is not of whole lattice vectors, and the lattice generated in the deformed region is the same as in the parent lattice but in a twin relationship, see Figure 6b. Another observation is that the atoms in each plane is moved forward by the same amount relative to those of the plane below, which is in contrast to slipping.

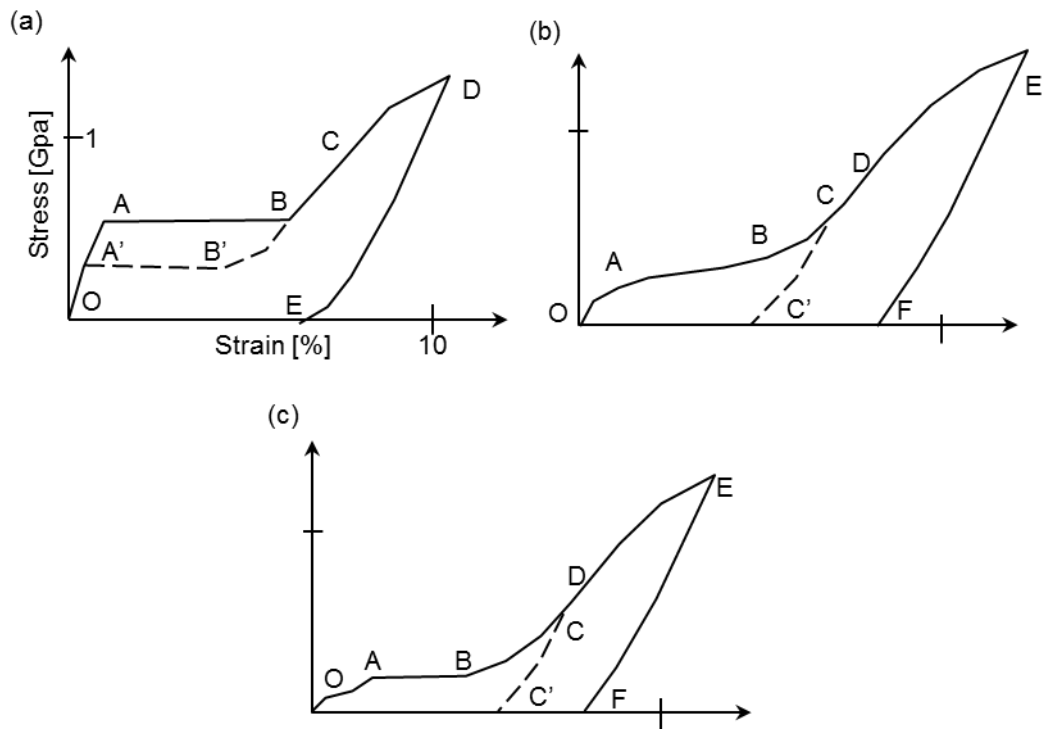


**Figure 7:** Schematic illustration of the NiTi stress-strain responses of NiTi wire in tension divided into areas of different deformation types (A-F). Initial respective unstressed phase and test temperature: (a) B2 and 70°C; (b) B19' and 10°C; (c) R-phase and 10°C (Shaw & Kyriakides, 1995).

Figure 7 shows the schematic diagram of stress-strain responses of NiTi wire at different temperatures and initial phases performed by Shaw & Kyriakides 1995. In Figure 7a the test temperature is above  $A_f$  so the parent phase (initial phase) is of simple cubic B2 lattice. In the first loading region (O-A) the stress causes only elastic distortion in the structure, but at some critical level (around A in Fig. 7a) it becomes unstable and the monoclinic B19' martensite is formed. This switch results in a macroscopic elongation brought on by the stress. If the test is performed under displacement control this transformation occurs under constant stress (plateau A-B). If the stress is released at point B in the Figure 7a the movement would follow the dashed B'-A' line showing that at some level (around B') the material will retransform to parent phase, referred to as superelasticity. Beyond point B, at which most of the material has transformed into martensite, deformation requires an increase in stress. At B-C the deformation is elastic distortion (detwinning) of the martensite and some due to martensite formation. At C-D the truly plastic deformation occurs as the martensite starts to slip, and upon unloading, more than 6% residual elongation will be present. The drop of elongation D-E is due to the presence of pockets of martensite able to transform back to the parent lattice.

Figure 7b shows the stress-strain response of a NiTi sample quenched (-196°C) and left to warm until room temperature. The martensitic microstructure formed by this heat treatment differs from the

stress-induced martensite of Figure 7a. The NiTi in 7b has variants of martensite configurations, which are rotations and/or mirror images of one another. They have coherent intersections although a local orientation difference is present, and are called twin boundaries. Movement of these twin boundaries is called detwinning, which implies to the straightening-out of the martensite lattice.

At O-A-B in Figure 7b, the detwinning takes place, first in the crystals favourable aligned to the direction of loading, second in the rest of the crystals at higher stress (B-D). The point D represents a fully detwinned material and further elongation causes slipping. Unloading at e.g. C-C' results initially in an elastic recovery, but the temperature needs to be raised to above  $A_f$  to fully recover the material.

Since the material used in these tests were at R-phase at room temperature, the test with initial R-phase lattice, see Figure 7c, need no heat treatment. In the starting region of the test (O-A), the variants of the R-phase are detwinned. The deformation in this starting region is significantly smaller than the deformation that can be accommodated by the monoclinic B19' martensite of Figure 7b. This fact is the reason for the transformation into B19' martensite (plateau A-B). Both during loading (B-C-D-E) and unloading (C-C' and E-F) the events taking place are very similar to those described for Figure 7b.

#### **2.2.4 Applications**

The applications of NiTi alloys can be divided and covered by the designation of four groups: superelastic devices, constrained recovery devices, martensitic devices and actuation devices (ASM Desk Editions, 2012).

As have been seen above NiTi has the ability to absorb large amounts of strain without any residual strain upon stress removal. Compared to steel, the elasticity is almost ten times higher for NiTi. Apart from this, the material has excellent torqueability and kink resistance which is important for e.g. medical guidewires and eyeglass frames. These guidewires can follow e.g. small blood vessels in their almost impassable spread. As can be seen in Figure 7, the NiTi also provides a rather constant force over a large range of strain. This is a sought for feature in arch wires used in dental care, since this improves the comfort for the patient.

Hydraulic pipe couplings can be made of NiTi. By manufacturing these cylindrical sleeve fittings a bit smaller than the tube they are made to join, the installer can expand them while martensitic, and upon warming shrink them by returning to the parent phase. This innovation of constrained recovery device, is in many ways superior to a weld if not at least an alternative.

Due to the energy absorption characteristics of the martensite's twinned phase structure, it has excellent damping characteristics. Also, the martensitic form of NiTi has remarkable fatigue resistance. Finally, the ease of deforming this phase with subsequent heating and thereby full return to parent shape, makes it useful for e.g. vibration dampers, bendable surgical tools for open heart surgery, and highly fatigue resistant wires.

As the name depicts, shape memory actuation devices benefit from the shape memory effect which is explained in subchapter 2.2.2. The devices can be constrained fully, partially or without any constraint to provide a force, work or recovery, respectively. The transformation temperatures, as have been mentioned before, can be adjusted to fit the situation precisely and for medical care a common actuation temperature is around 37°C, i.e. the human body temperature. Examples of these devices are vascular stents, blood clot filters (a NiTi wire is shaped into an anchor upon choice and catch passing clots inside the blood vessel) and coffee pot thermostats.

## 2.3 Powder metallurgy

This subchapter aims to present the general principles to understand powder metallurgy (PM) and its use for accomplishing bulk porous samples of NiTi.

### 2.3.1 General principles of powder metallurgy

The main principles of PM are today well developed thanks to the requirements from technical development of high-performing and cost-efficient materials (Ekbohm et al., 1995). The common principles for all subgroups of powder technology can be summoned in three steps as manufacturing and processing of powder, forming of the powder into a so called green body and a subsequent heating of it to high temperatures but still below the melting temperature of the main component, so called sintering. Special approaches (see further below) where heat (the sintering) and pressure are simultaneously applied include so-called hot isostatic pressing (HIP) or hot pressing. Metal powder for PM can mainly be produced in two ways: mechanically/physically or chemically (Yule & Dunkley, 1994). The most commonly used powder production methods are atomization by gas or water, milling, electrolysis and chemical methods including reduction of oxides. The atomization methods are perhaps the most versatile with the possibility to create powder of sizes 10-1000  $\mu\text{m}$ . The method is based on powerfully blowing gas or water onto a melt seeping from above into the atomization chamber, causing it to form droplets that rapidly solidify into powder. The two main differences of gas and water atomization is that the gas atomization produces more spherical shape particles with less oxide, which can be both advantageous and disadvantageous depending on use.

Powder forming is divided into two subcategories: powder shaping and compacting. The powder shaping technologies can be summoned through binder-assisted extrusion, used for relatively simple and long shapes, injection moulding, used for small complex components, slip casting, used for very large structures, and tape casting to form flat sheets (German, 1998).

Powder compacting is, unlike powder shaping, causing particle deformation. This deformation is achieved by applying high pressure through various methods. This pressure packs the powder and reduces porosity. The pressure is applied either by uniaxial die compaction in a rigid die or by isostatic pressing. In the first case, apart from pressure application, temperature increase can also be used and can be categorized into three different uniaxial die compaction types: cold, warm and hot. Regarding isostatic pressing, a flexible mould is used, which is submerged in a subsequently pressurised fluid enabling the pressure to be applied on all surfaces. Within isostatic pressing, either cold or hot isostatic pressing can be used depending on the situation (CIP and HIP, respectively).

Sintering of metal powder basically occurs by neck growth at particle-particle contacts driven by the overall minimizing of excess surface area. Often, the solid state sintering, as in the case of die compacted materials when having high initial relative density, is designed in such manner that shrinkage is avoided to keep dimensional tolerances. Only if initial relative density is lower and metal particle size is small as in e.g. metal injection moulding (MIM), the solid state sintering is run to near full sintered density. Besides general solid state sintering, there are four general types of sintering, depending mainly on temperature and material properties. For all of them, the powder particles need to be in contact with each other to achieve an efficient sintering. The first, liquid phase sintering implies having a lower melting temperature powder causing this to melt and enable the other higher melting temperature powder to rearrange and densify during sintering. The second, transient liquid phase sintering, resembles the liquid phase sintering but with the difference that the liquid alloys with the base powder, so the liquid is only present for a brief moment. The third, high-temperature sintering, means that the temperature is risen to levels close to the melting temperature of the powder enabling microsegregations of lower melting temperature to melt and accelerate densification. The fourth,

reactive sintering, relies on the flexibility of powder blends enabling it to contain such components that a self-propagating reaction occurs.

The properties of the finished product are mainly depicted by the properties of the powder and the forming and heating processes, but post-sintering processing is also possible (Ekbom et al., 1995). Provided that porosity is minimized, the strength of the components produced is often at least as good as made by conventional manufacturing methods. The main advantages of PM are that segregations are avoided, some processing operations are left out, the required structure is generated, material volume and energy is saved, all motivating the use of the PM manufacturing method from a sustainable point-of-view.

### 2.3.2 NiTi in powder metallurgy

Since powder metallurgy enables production of bulk materials without reaching or passing its melting temperature, NiTi with its relatively high melting temperature is suitable for PM (Bansiddhi et al., 2008). Since pre-alloyed powder generates an extra step in the powder manufacturing stage, elemental powder has been of majority use. However, using elemental powder often generates residuals of non-equiatomic Ni-Ti phases which are difficult to remove. The solution is to use pre-alloyed powder of equiatomic NiTi.

Pre-alloyed NiTi powder has been used to create porous NiTi in both conventional sintering and argon expansion (Bansiddhi et al., 2008). Other than these techniques, a space-holder powder has been used to consolidate and form pores upon removal. For example NaCl (common salt) and NaF were used for hot isostatic pressing and metal injection moulding, respectively. However, till date, use of starch as a space-holder for either elemental or pre-alloyed powder has not yet been explored to produce porous structures.

## 2.4 Starch consolidation

A group of the techniques of powder shaping is called “Direct-consolidation techniques” (DCT) (Magalhães et al., 2003). The basic principles are consolidation without powder compaction or liquid removal to form rigid components from powder suspensions or slurries. When the slurries are in initial state, they should be homogeneous (Lyckfeldt & Ferreira, 1998). This implies that when locked in the solid state, favourable conditions for homogeneous shrinkage and no segregation effects should be present upon sintering.

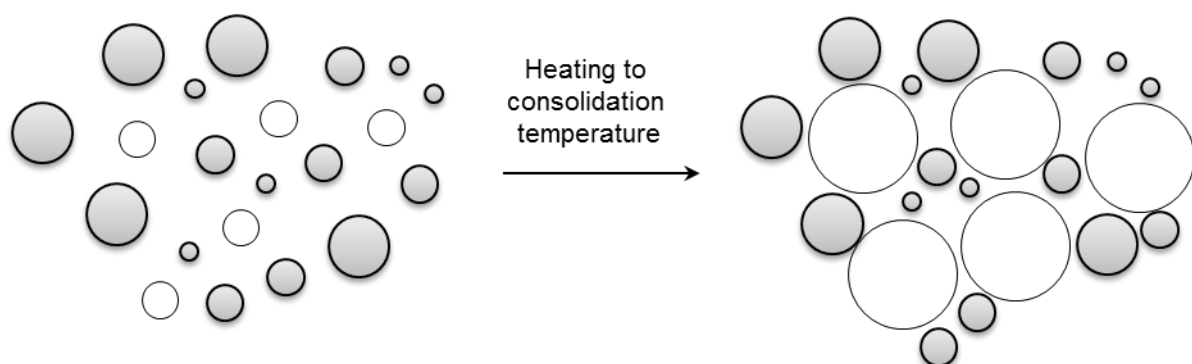


**Figure 8:** The principle of starch consolidation. Slurry (left) with unconsolidated starch particles (white) and metal powder particles (grey) is heated to the consolidation temperature at which the starch consolidates (Hoseney, 1998).

In this thesis the water-based starch consolidation method was used. This method was developed by Lyckfeldt & Ferreira in 1997 and the use of this forming method here was a blend of the author’s own

experiences as the work progresses, the work done by the developer and also from Magalhães et al. in 2003. This DCT process uses a property of all starches; when heated in excess of water the granules will swell (gelatinize) by absorbing water, see Figure 8. This locks in the metal powder in a matrix forming a green body (Lyckfeldt & Ferreira, 1997). The starch is both consolidator/binder and pore former. However, additional ingredients and procedures were used in this thesis' starch consolidating and these are described in the subchapter 3.2.2.

### 3. METHODOLOGY

This chapter presents the material, methods used and experiments performed in this thesis.

#### 3.1 Powder

The NiTi powder used in this thesis project was pre-alloyed Ni–44wt.%Ti (approx. Ni–49at.%Ti), gas-atomized with argon using the Nanoval process and according to supplier (Nanoval GmbH & Co. KG, Germany) having an as-received  $A_f$  of between  $-15$  and  $-10^\circ\text{C}$ . Gas-atomizing means geometrically that the powder is mainly or solely of spherical shape. The powder had a particle size of below  $300\ \mu\text{m}$  and a  $d_{50}$  of  $110\ \mu\text{m}$ .

#### 3.2 Sintering

All sintering trials were carried out with a horizontal alumina tube in a Carbolite STF15/75/450 furnace heated by silicon carbide heating elements in an argon gas of different supply procedures and purities, see Table 2. The temperature was measured and digitally logged with type S thermocouple and thermometer. The sintering temperature was selected based on loose powder sintering trials performed to make sure that densification was enough, but still tentatively maintaining an open porosity.

##### 3.2.1 Loose powder sintering

**Table 2:** Assembled data of all sintering trials.

	Argon gas purity	Samp-les *	Heating rates **	Pre-hold temp. $T_{\text{pre-hold}}$	Pre-hold time $t_{\text{pre-hold}}$	Dwell temp. $T_{\text{dwell}}$	Dwell time $t_{\text{dwell}}$	$T_{\text{Ar Off}}^{***}$
	[at.% Ar]		[ $^\circ\text{C}/\text{min}$ ]	[ $^\circ\text{C}$ ]	[min]	[ $^\circ\text{C}$ ]	[min]	[ $^\circ\text{C}$ ]
<b>1</b>	99.990	P	9	105	5	1270	90	250-300
<b>2</b>	99.999	"	18	None	None	1255	100	<100
<b>3A-B</b>	"	S	"	415	25	"	"	"
<b>4A-C</b>	"	"	"	"	"	"	"	"
<b>5</b>	"	"	"	"	"	"	40	"
* P: Powder sample, and S: Starch consolidated sample.								
** Heating rates were approximately the same before and after the eventual pre-hold.								
*** Temperature at which the argon flow was turned off during cooling.								

The loose powder sintered samples 1 and 2 (c.f. Table 2) were produced by sintering the powder in crucibles of simple heat-resistant ceramic and alumina, respectively, following the schematic temperature-time profile in Figure 9. The powder was poured into the crucibles and some tapping was implemented to ensure a total fill-up of the containers. Boron nitride spray was applied to the inner surfaces of the crucible to simplify post-sintering demoulding. A pre-hold at just above  $100^\circ\text{C}$  was added for sample 1 to enable the low-porosity ceramic crucible to fully dry out of water.

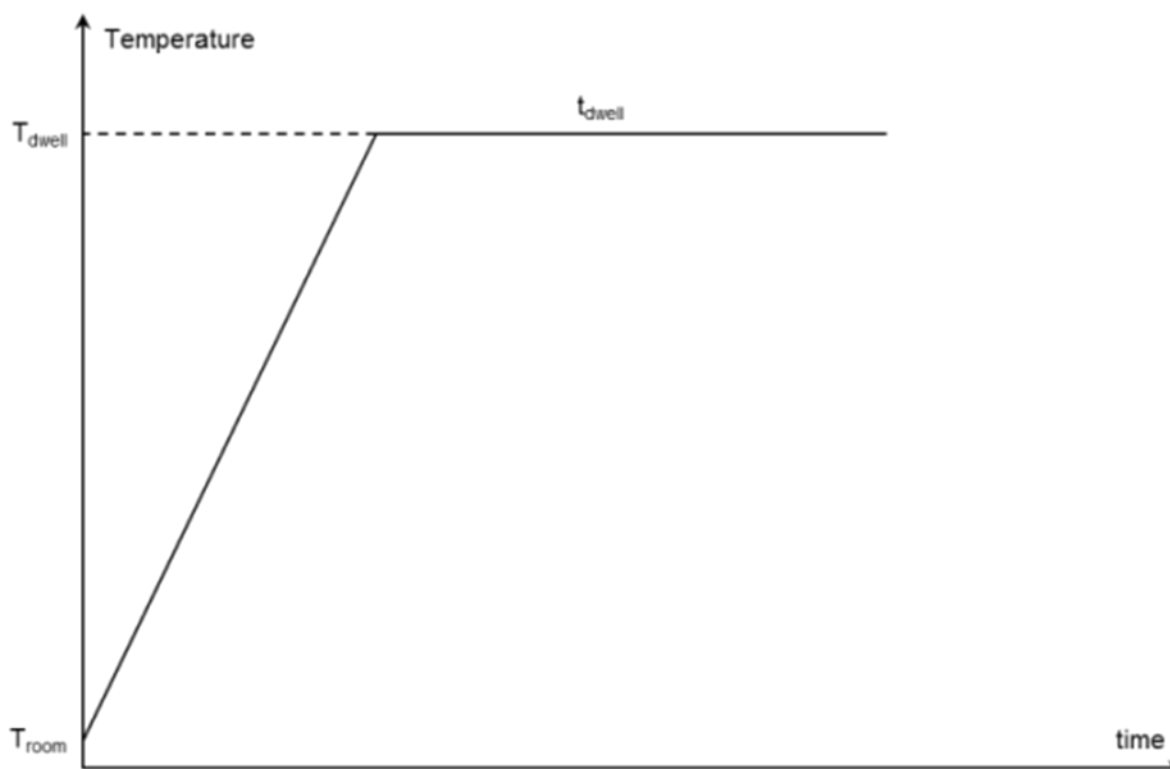


**Figure 9:** The schematics of the time-temperature sintering process diagram for conventional samples.

### 3.2.2 Starch consolidation and sintering

**Table 3:** Starch consolidation sample preparation data. The data is presented as the amounts that are added to the blend, this to simplify reproduction of the preparations.

Trial	1-octanol	Thickener	Starch	NiTi powder	Dispenser	Main dwell time $t_{dwell}$
	[drops/100 ml water]	[wt.% water]	[wt.% liquid*]	[vol.% slurry**]	[wt.% water]	[min]
3A	10	2	11	60-65	10	100
3B	"	"	"	"	"	"
4A	"	"	7	"	"	"
4B	"	"	11	85-90	"	"
4C	"	"	"	60-65	3	"
5	"	"	"	"	10	40
* Liquid is water and dispenser						
** Slurry is water, 1-octanol, thickener, dispenser and starch						

The sintering of samples 3 to 5 (c.f. Table 3) were preceded by production and consolidation of the powder-containing slurry and subsequent starch consolidation following the recipes presented in Table 3. Samples 3A and 3B represent reference samples according to a starting recipe. Samples 4A-C and 5 are variants with different parameters (starch level, powder loading, dispenser level, processing time).

The production was initiated by mechanically mixing a cellulose ether based thickener in powder form (Methocel A4M, Dow, Germany) and liquid antifoaming agent (1-octanol) with tap water. The thickener is added to avoid settling of the metal powder and thus to promote homogeneity later on. The mixing was performed intensely for 15 min to improve thickener dissolution. Disregarding bubbles created, the blending was less violently continued until the thickener was fully dissolved. The liquid polycarboxylic ether based disperser (Glenium 51, BASF AB, Sweden) was then added and dissolved followed by an addition and dissolution of modified potato starch powder (Microlys 54, Lyckeby Culinar AB, Sweden) under continuous blending. The disperser is added to avoid agglomeration of the metal powder and hence promote homogeneity later on. The NiTi powder was then finally added and hand-blended into the mix to create the sludge.

This sludge was then poured into disc-shaped sample moulds and evacuated by subjecting it to a pressure decrease to around 15 kPa for 5 min. This was performed to remove the bubbles left in the slurry from the intense mechanical mixing. The pressure level was chosen to keep the water in liquid phase and avoid entering the vapour phase. Following the evacuation, the samples were put into a pre-heated oven of 75°C for at least 120 min to gelatinize the starch. The samples were thereafter placed in a freezer (approx. -20°C) to solidify them, which enabled the subsequent demoulding. A full drying of the samples on glass surface at room temperature completed the sample preparation prior to sintering. A dried sample next to its mould can be seen in Figure 10.

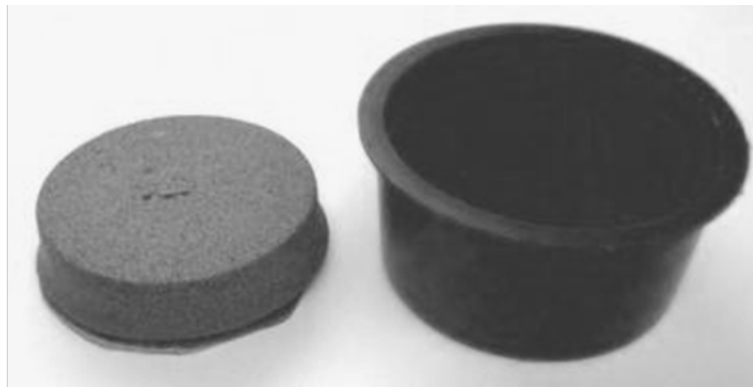


**Figure 10:** A demoulded and fully dried out sample next to its mould. The sample is around 28 mm in diameter and 10 mm in height.

When sintered, the starch consolidation samples were placed on dense heat-resistant ceramic plates in argon atmosphere (cf. Table 3). The pre-hold temperature of above 400°C used for starch consolidated samples, see Figure 11, was implemented to enable a maximal burn-out of the starch before actual sintering (Lyckfeldt & Ferreira, 1997). The sintering was performed at 1255°C. The dwell time was chosen as a result of experience generated during the realisation of this project.

After dwelling, the furnace was turned off and the sample was left to cool in argon atmosphere inside the oven until it reaches an ambient temperature. The argon atmosphere is essential to minimize oxidation of the highly reactive titanium (Buehler, 1963).

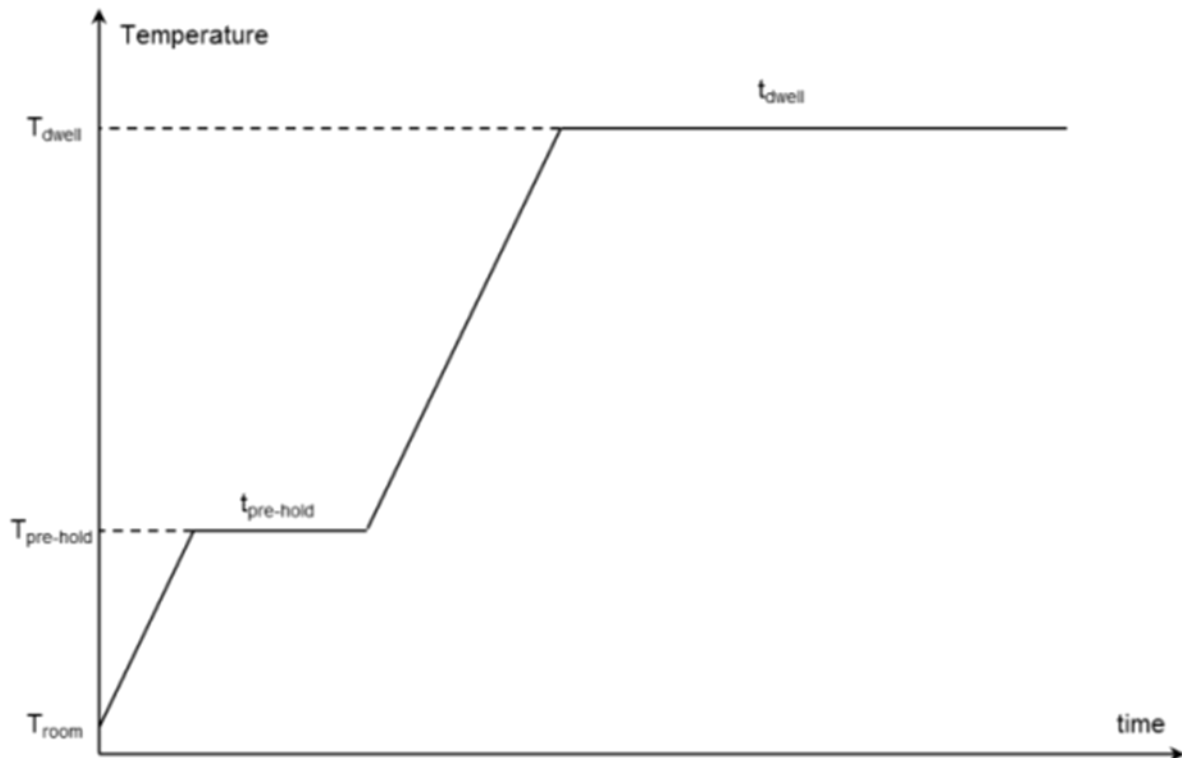


**Figure 11:** The schematics of the time-temperature sintering process for starch consolidated samples with two ramps of the same heating rate [ $^{\circ}\text{C}/\text{min}$ ].

### 3.3 X-ray diffraction

In order to obtain the structural and phase evolution, X-ray diffraction studies were carried out. The powder and the samples 2, 3A and 4B were analysed by means of a Bruker AXS D8 Advance X-ray diffractometer with  $\text{CrK}\alpha$ -radiation (wavelength  $\lambda = 0.229 \text{ nm}$ ). The data found in available powder diffraction files were compared to the XRD patterns to enable identification of the phases.

### 3.4 Scanning electron microscopy

The polished and unetched samples 2, 3A and 4B was analysed using LEO 1550 Gemini high resolution scanning electron microscope (SEM) equipped with energy-dispersive X-ray spectroscopy (EDX). The beam voltage used was 20 kV for samples 2 and 4B, and 10 kV for sample 3A.

### 3.5 Electrical discharge machining

The cylindrical samples were cut out from the samples 3 to 5 by wire electrical discharge machining (EDM). This was made to enable compression tests. The cylinders were 4.45-5.23 mm in height and 2.54-2.65 mm in diameter. These cylindrical samples were extracted both horizontally and vertically, to enable a possible differentiation due to potential anisotropy of sintered samples, see Figure 12.

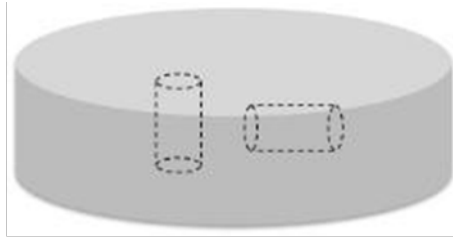


**Figure 12:** Illustration of test piece extraction by EDM from a sample, both vertically (left dashed cylinder) and horizontally (right), c.f. Figure 10.

### 3.6 Porosity measurements

In this subchapter the measurement of relative apparent density of powder and apparent porosity of sintered samples is presented. This was made to enable a comparison. The solid was in both cases assumed to be composed of pure NiTi and thereby having a density ( $\rho_{NiTi}$ ) of 6450 kg/m<sup>3</sup> (Buehler & Wiley, 1961). And the calculations were made with the use of the porosity equation:

$$Porosity [\%] = 100 \cdot \left(1 - \frac{m_{sample}}{\rho_{NiTi} \cdot V_{sample}}\right) \quad (Eq.1)$$

where  $m_{sample}$  and  $V_{sample}$  are the mass [kg] and volume [m<sup>3</sup>] of the samples measured. The porosities measured are the sum of open and closed porosities as this method does not allow a differentiating of the two.

#### 3.6.1 Powder

Powder was poured into a measuring cylinder and carefully measured for volume and weight. This was performed to generate data to enable calculation of the as-poured value. After about 30 s of tapping the new volume was read to enable calculation of the tapped value with the above porosity equation. An average of five measurements was taken as the respective apparent porosity value. It should be noted that the porosity value obtained in this manner does not reflect a real porosity of the powder itself. Instead, it is a measure of the packing of powder depicting the unfilled space in between the metal particles in a powder lot.

#### 3.6.2 Sintered samples

The pieces cut from the precision saw from sample 1 and 2 together with EDM cut cylinders from sample 3 to 5 were weighed and measured with a micrometer for volume. An average porosity (open and closed together) for each sample was calculated from its cut-outs.

### 3.7 Microhardness

Macro-hardness tests were not usable to depict microstructure hardness as the samples are porous. Instead, Vickers micro-hardness tests were performed on densified locations on cross-sections of the samples to get a sense of its yield strength. The load was set to 100 g and the hold time to 12 s and an average of ten values was set as the Hardness Vickers (HV) value.

### 3.8 Mechanical testing

Compression tests were performed in a displacement controlled (0.05 mm/s) servohydraulic testing machine (Instron 8032, US). Prismatic samples with near-quadratic cross section were cut from samples 1 and 2 with a precision saw for the purpose of compression testing. As mentioned before, cylindrical test pieces for compression test were obtained from sample 3 to 5 by wire EDM.

The test pieces from samples 1 to 5 were measured and then subjected to compression until failure of test piece. The force, extensometer, time and displacement data were simultaneously recorded using computer, enabling a subsequent plotting of engineering strain vs. stress using the test piece cross-sectional area and length. Also, for each sample the data was used to calculate  $s_u$ , the maximum pressure applied on the test piece, E-modulus, the slope of the initial linear portion of the engineering stress-strain curve,  $s_y$ , the compressive yield strength (offset 0.2%),  $s_f$ , stress at fracture and  $e_f$ , strain at fracture.

Before compression testing, some extra test pieces from samples 4A and 5 were placed in an oven at 130°C for 20 min and then allowed to cool to room temperature and hold for >1 hour. This was performed to anneal them and try reaching a maximum B2 phase structure. Also, some other extra pieces from samples 3A, 4A and 5 were placed in liquid nitrogen (max -196°C) for 5 min and then allowed to warm in room temperature and hold for >1 hour. This quench step was performed to try reaching a maximum martensitic structure. These two treatments were done to enable subsequent compression tests of test pieces with possibly altered structure in comparison to untreated test pieces from sintered samples. The compression tests of the heat-treated test pieces were performed in the same way as the untreated test pieces.

Test pieces from samples 3B and 5 were for ten cycles compressed to 5.5 and 5.0 kN, respectively, and then released. These tests were performed to generate engineering stress vs. strain plots for cyclic loading. Following the cyclic loading, the samples were tested again, preceding being inserted into an oven at 130°C for 20 min. The treatment was made to confirm the shape memory effect and enable measure of the recovery of residual strain.

## 4. RESULTS

This chapter shows the main results generated in this master thesis project.

### 4.1 Sample production

In this subchapter the sintered products will be presented in the form of ocular observations and optical microscopy.

#### 4.1.1 Appearance of loose powder sintered samples

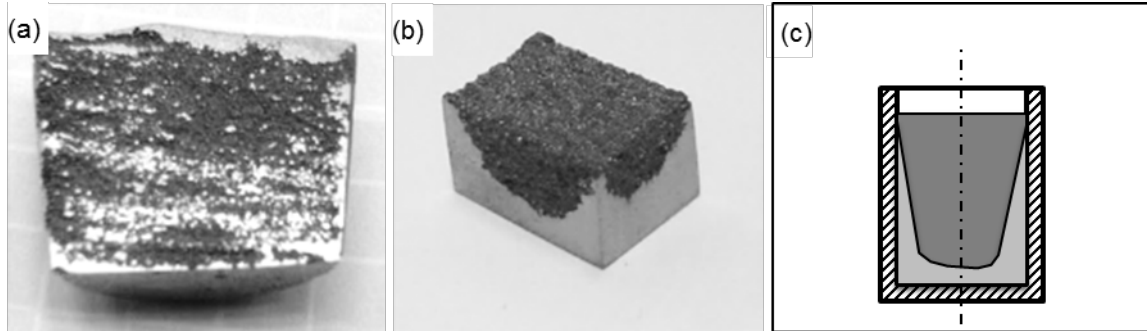


**Figure 13:** a) Photo of sample 1 demoulded and cut through its center. The visual bottom part of the sample photo is the sample bottom. The sample is around 19 mm wide (diameter) and 13 mm in height. b) Photo of a cut out bottom piece of sample 2 where the denser and more porous volumes can be seen, c.f. c) Figure. The object is around 10x5x5 mm. c) Schematic illustration of the cross-section of sintered powder in a crucible (striped area) with line of symmetry (dash dot line, since cylindrical crucible). The denser volume (light greyish) and the more porous structure (dark greyish) formed upon sintering.

Loose powder sintered samples 1 and 2 were removed from their respective crucibles without fracture. Sintering was achieved at least partially throughout the whole samples. In Figure 13a a cross-section of sample 1 can be seen. The surface has been polished and the metallic coloured parts represent better fastened particles which has sustained polishing, whilst the darker parts represent areas where particles have fallen off due to polishing, i.e. not being able to sustain the abrasion of the polishing step.

In sample 2, there were two volumes of different characteristics (see Fig. 13b). The lighter shinier part of the sample comprises denser (less porous) material as compared to the other, more porous part, showing darker blackish appearance. These different volumes were located in the sample according to the illustration in Figure 13c, which is a rotational symmetric view across the cylindrical crucible used for sample 2. As the shinier volume is smaller and almost fully dense, the porous volume was used for porosity measurements, hardness and compression tests. The final reason for the different sintering behaviour of the different parts has not been clarified. One tentative reason can be interaction with the crucible surface.

#### 4.1.2 Appearance of starch consolidated samples

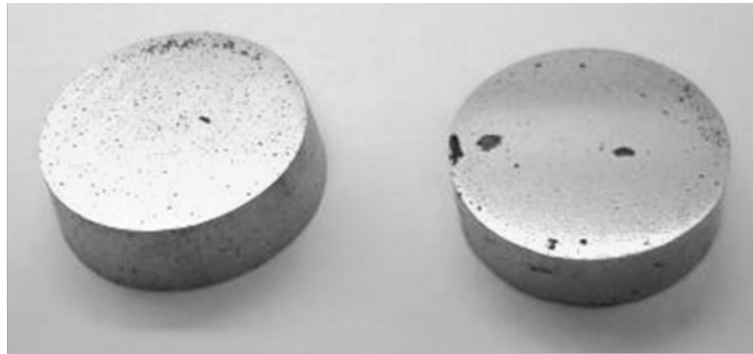


**Figure 14:** Starch consolidated samples 4B (left) and 4C (right) after being polished post-sintering. The samples are of sizes around 26 mm in diameter and 8 mm in height. Dark spots and areas are cavities and/or porosities.

The starch consolidated samples 3 to 5 were all sintered into puck-shaped samples of sizes around 30 mm in diameter and 8 mm in height. The surfaces were upon removal from the furnace rugged and dark, but upon polishing a metallic shiny surface can be displayed, see Figure 14 above. All samples were more or less concave after sintering and the sides were generally horizontal except for 4B which had a broadened base.

#### 4.2 Geometrical and Porosity measurements

**Table 4:** The porosities of powder and samples.

	Powder		Samples							
	As-poured	Tapped	1	2	3A	3B	4A	4B	4C	5
Porosity [%]	40	34	24	34	26	7.0	33	33	36	12

The results of the geometrical and porosity measurements of powder and sintered samples can be seen in Table 4. One notable comparison is that sample 4C, has a higher porosity than the tapped powder itself. Samples 2, 4A and B also have high porosities, but lower than the as-tapped powder, while 3B and 5 clearly have lowest porosities, revealing significant shrinkage.

#### 4.3 Microhardness

**Table 5:** Micro-hardness Vickers average values for the sintered samples.

Samples (HV 100 g)							
1	2	3A	3B	4A	4B	4C	5
390	390	490	500	490	440	500	420

The results of the micro-hardness tests can be seen in Table 5. The starch consolidated samples (3 to 5), see Table 3, have higher HV value than the loose powder sintered (1 and 2). The average hardness values reveal that the starch consolidated samples exhibits 22% higher hardness as compared to the loose powder sintered samples.

## 4.4 SEM and EDX

This subchapter presents the results of scanning electron microscopy and the micro-analyses done with energy-dispersive X-ray spectroscopy.

### 4.4.1 SEM

In this subchapter the SEM imaging of cross-sections of samples 2, 3A and 4B are presented. These samples were selected to provide a comparison between loose powder sintered condition (sample 2) as well as sintered starch consolidated samples based on lower (sample 3A) and higher powder loading in the slurry (sample 4B), respectively.

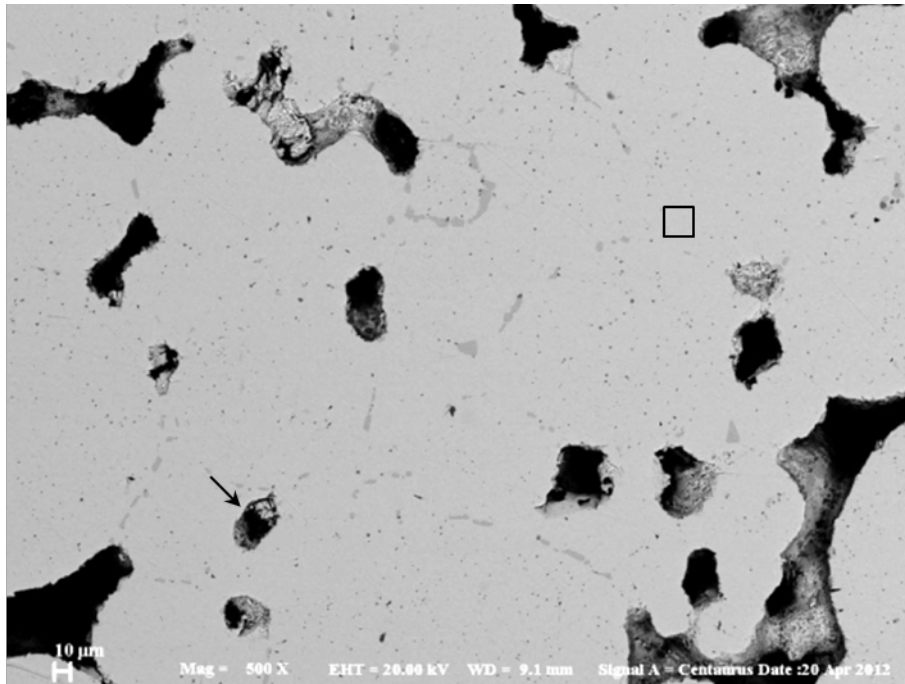


**Figure 15:** SEM image of dense volume from sample 2 with surface observations pointed out. Main matrix (square) and porosity (arrow).

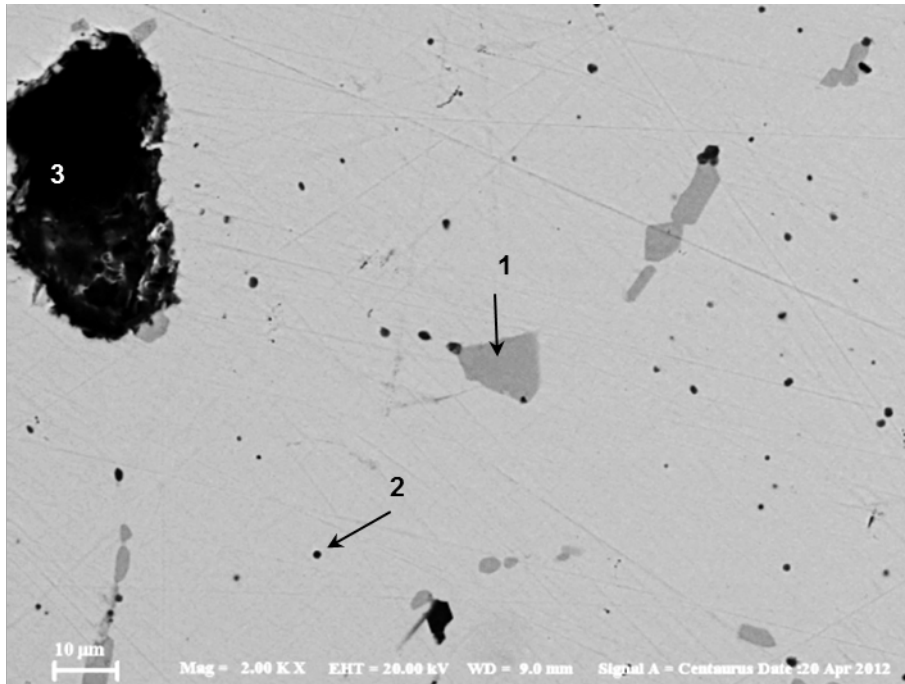


**Figure 16:** SEM image of dense volume from sample 2 with greyish area (arrow 1), blackish particle (arrow 2) and porosity (3).

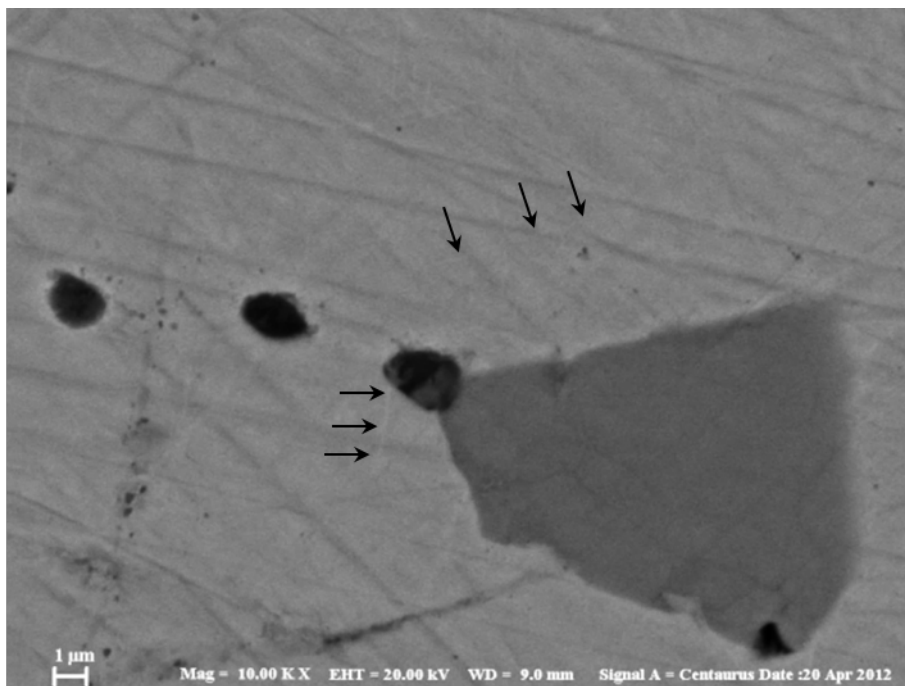


**Figure 17:** SEM image of dense volume from sample 2 with arrows pointing on thin whitish lines.

SEM images of the denser volume of sample 2 are shown in Figures 15-17. Figure 15 shows the overall view and reveals good particle bonding between particles in contact with one another (square) as well as large pores (arrow). Features appearing as dark greyish areas occur at particle boundaries and with certain shapes of up to 20  $\mu\text{m}$  of length (arrow 1) as shown in Figure 16. Also, there are blackish particles (arrow 2) of 1-2  $\mu\text{m}$  in size spread randomly across the examined section. In Figure 17, higher magnification imaging reveals the existence of thin whitish line-shaped features of approximately  $<100$  nm width and 4-5  $\mu\text{m}$  length (see arrows).

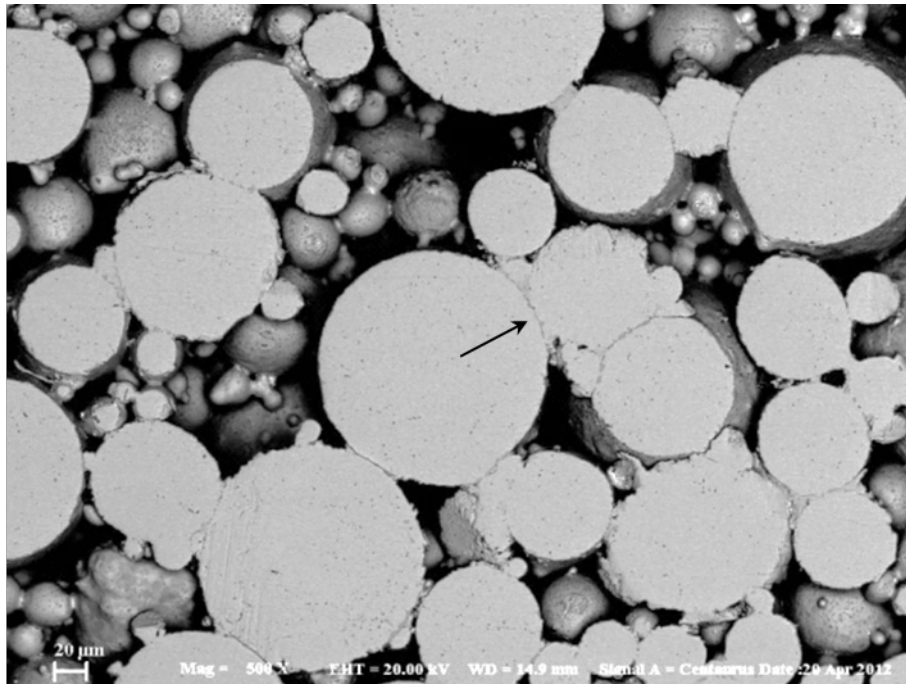


**Figure 18:** SEM image of porous volume from sample 2 with greyish area (arrow).

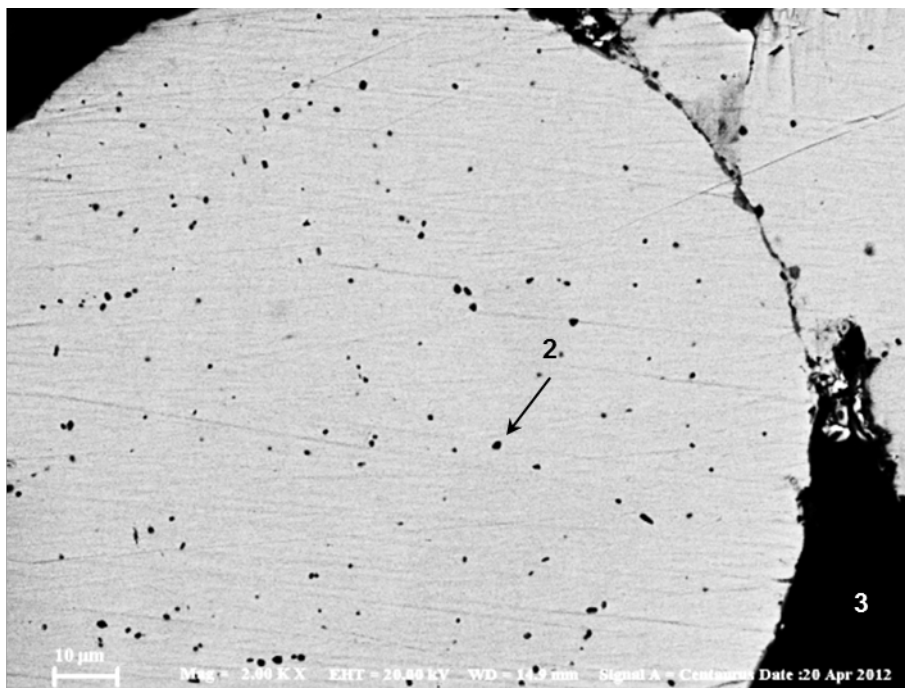


**Figure 19:** SEM image of porous volume from sample 2 with blackish particles (arrow 2) and porosity (3).

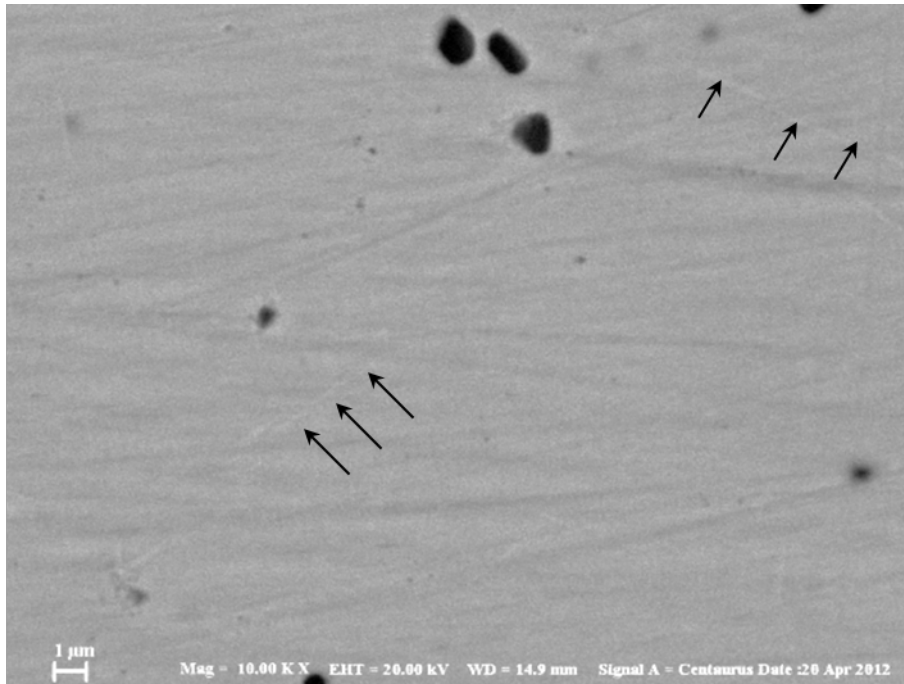


**Figure 20:** SEM image of porous volume from sample 2 with arrows showing thin whitish lines.

The porous volume of sample 2 is represented by the SEM images in Figures 18-20. The image at low magnification (see Fig. 18) shows the overview of the sintered structure, with evidence of good sintering of particles in contact, but with high porosity due to less good packing than in Figure 15. Arrow 2 in Figure 19 indicates the blackish particles also found in the dense volume. However comparing Figures 16 and 19, the amount of these blackish particles are higher in 16 than in porous volume of the sample. The arrows in Figure 20 indicate the thin whitish line-shaped features also found in dense volume with same size.

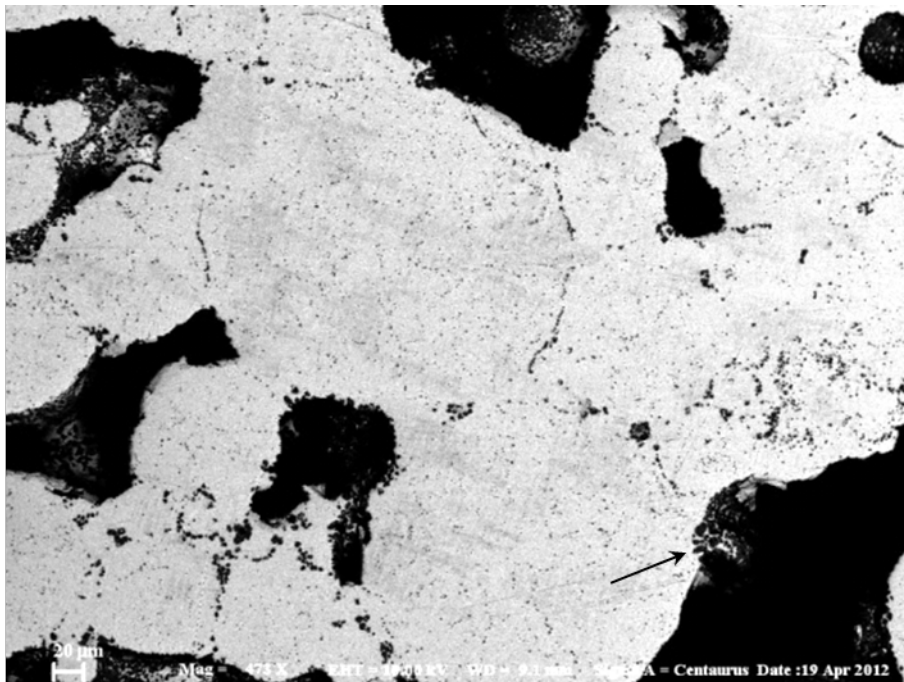


**Figure 21:** SEM image from sample 3A with non-polished powder surface (arrow).

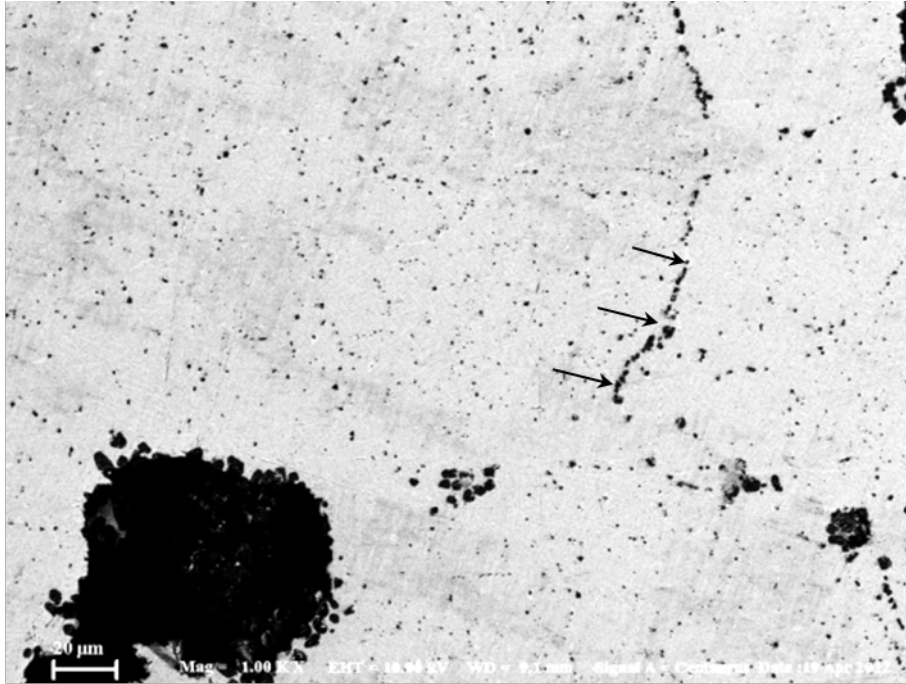


**Figure 22:** SEM image from sample 3A. Arrows indicating blackish particles surrounding a certain shape.

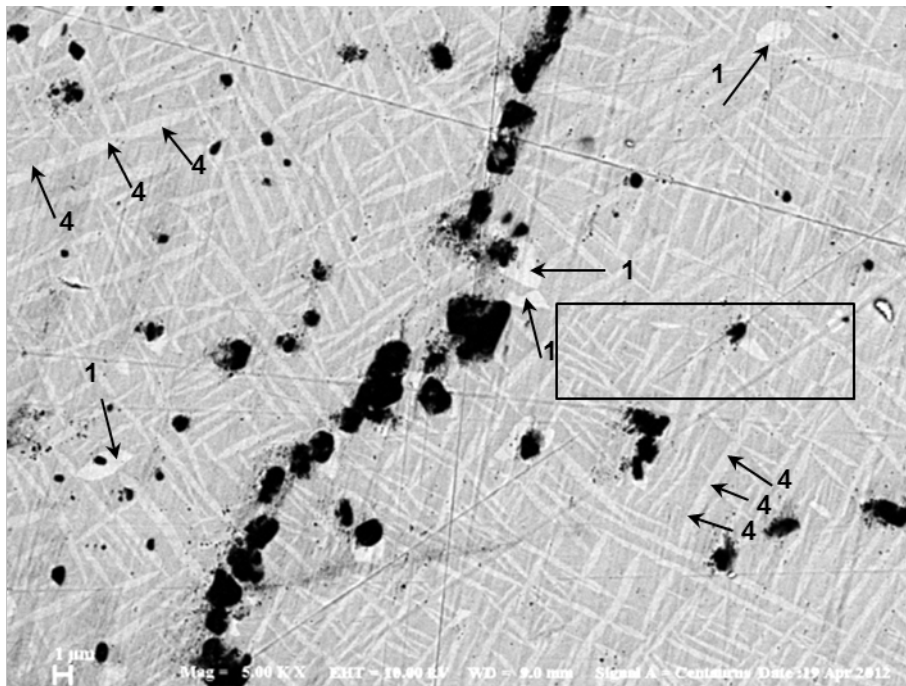


**Figure 23:** SEM image from sample 3A with areas of irregular shape (arrows 1) and oblong formations (arrows 4). Also a grain boundary can be seen diagonally crossing the rectangle.

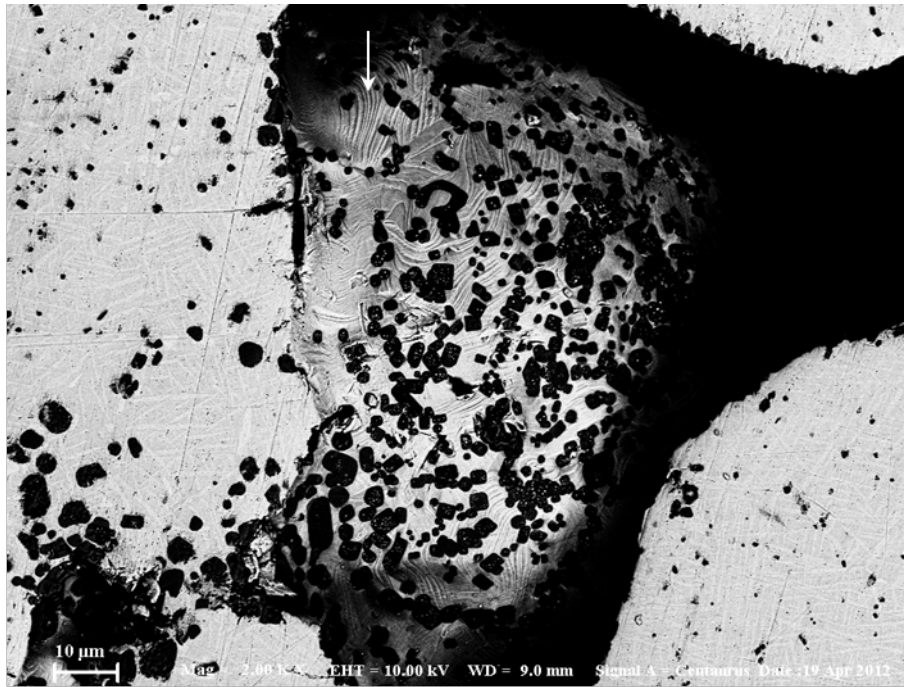


**Figure 24:** SEM image from sample 3A. White arrow indicates step-like formations on the non-polished surface. Also, blackish particles can be seen on both polished and non-polished surface.

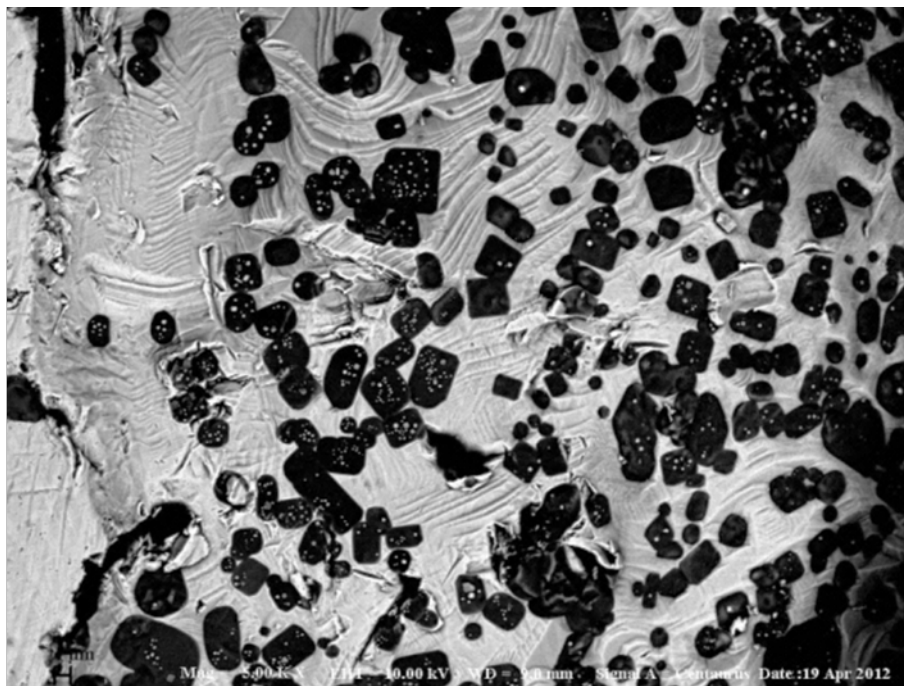


**Figure 25:** SEM image from sample 3A where the shape of the blackish particles can be seen clearly.

The SEM images of sample 3A, (starch consolidated, sintered) can be seen in Figures 21-25. Figure 21 shows an overview of polished surface with blackish particles (or pores) and untouched powder surface indicated by an arrow. Apart from large pores, arrays of blackish particles along the powder particles can be observed and are denoted by arrows in Figure 22. In Figure 23 oblong formations (arrows marked 4) of widths and lengths of ranging 0.2-1  $\mu\text{m}$  and 1-15  $\mu\text{m}$  respectively can be seen. Also irregular shaped inclusions of some  $\mu\text{m}$  in size can be found indicated by arrows marked 1 as well as prior particle boundary or grain boundary with precipitates, crossing diagonally in the inserted rectangle.

Figures 24 and 25 illustrate blackish particles of 2-3  $\mu\text{m}$  in size situated on non-polished powder surface as well as on the polished cross-section areas. Noticeable is the shape of these particles, they are often square or octagonal with every second side much shorter. Also, arrow in Figure 24 indicates step-like formations on the non-polished particle surface as also more clearly seen in Figure 25.

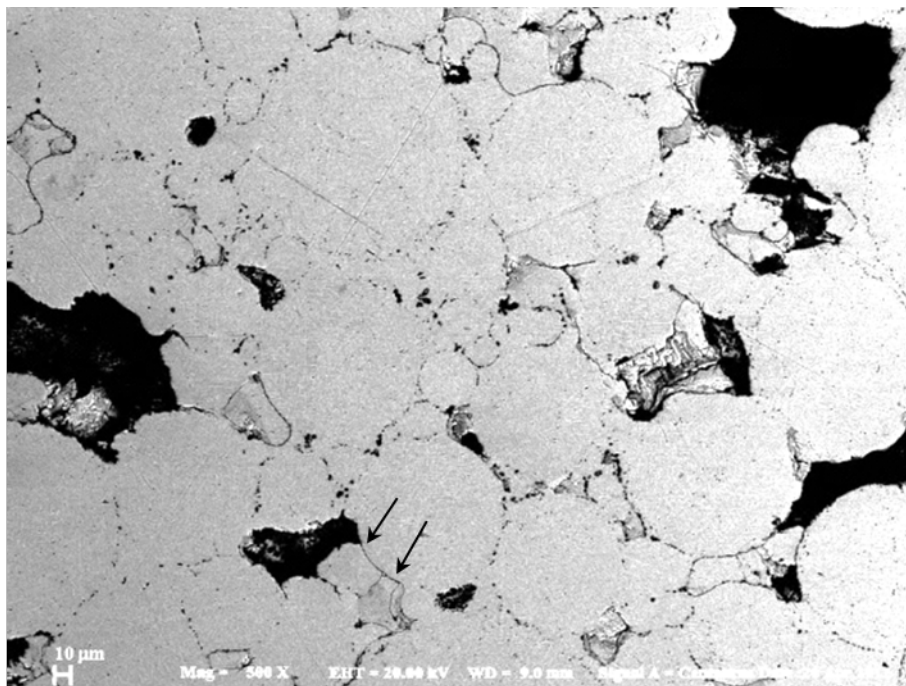


**Figure 26:** SEM image from sample 4B. Arrows indicate the agglomeration of blackish particles surrounding certain shapes alternatively weakly sintered powder particle borders.

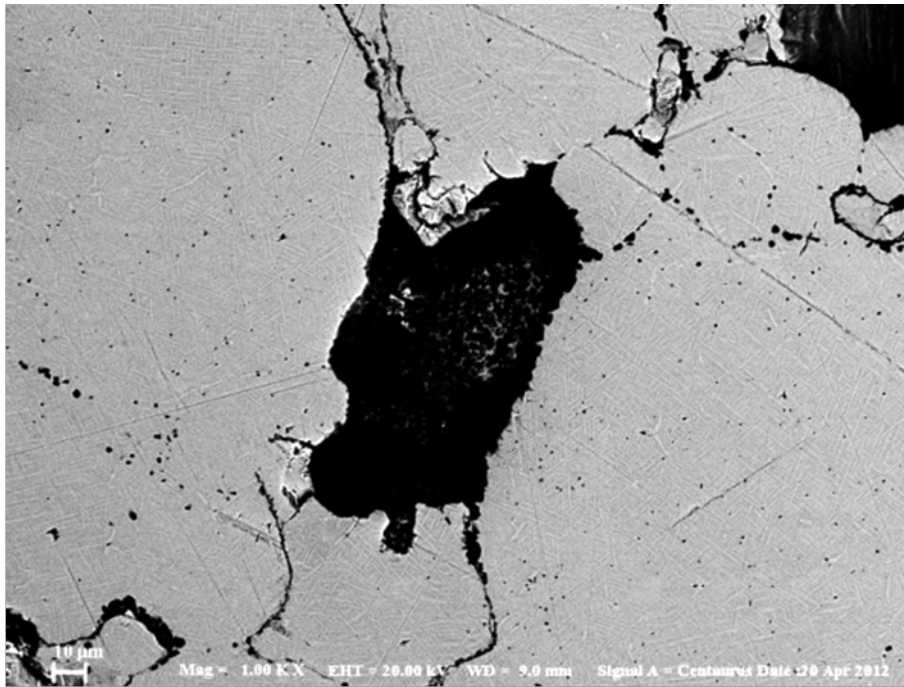


**Figure 27:** SEM image from sample 4B with oblong formations.

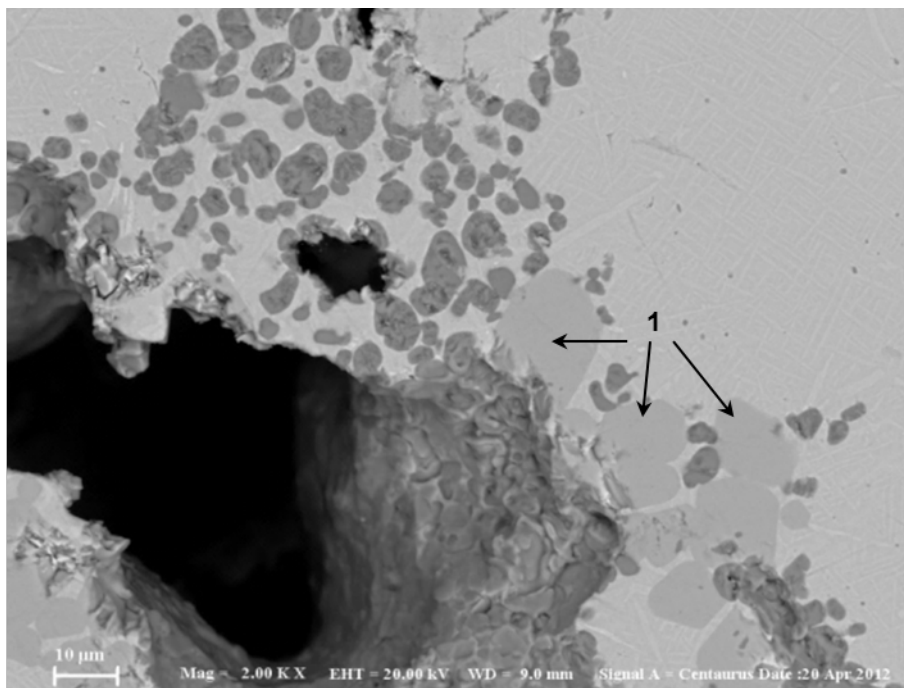


**Figure 28:** SEM image from sample 4B with dark greyish areas close to a porosity (arrows 1). Also an agglomeration of blackish particles can be seen in the upper middle part of the figure.

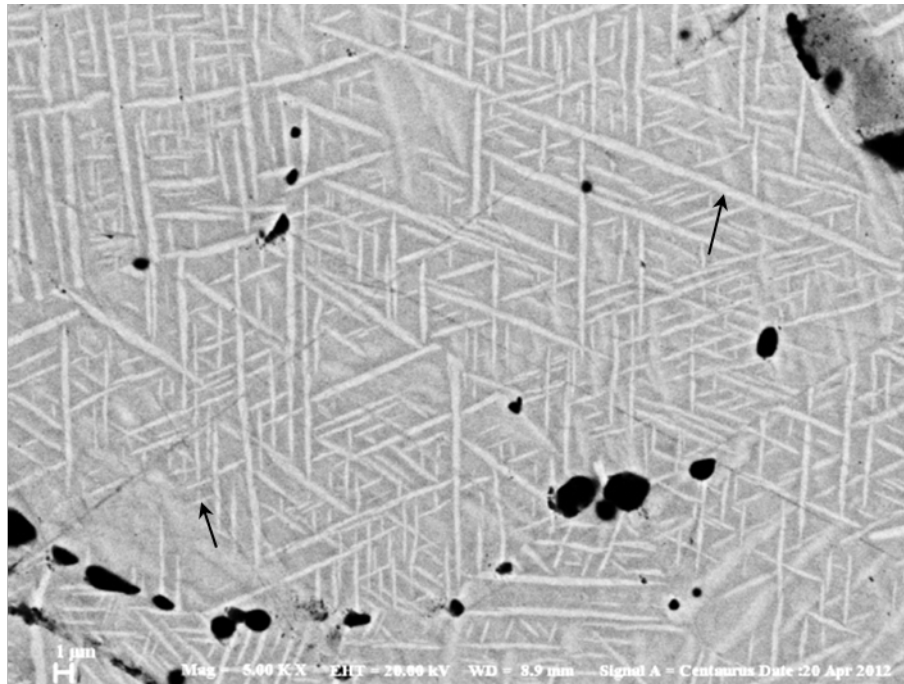


**Figure 29:** SEM image from sample 4B with oblong formations of varying sizes (arrows).

The SEM images of sample 4B can be seen in Figures 26-29. In Figure 26, the arrows indicate agglomeration of blackish particles, revealing poor interparticle bonding, which is not observed for the other samples. The oblong precipitates can be observed for sample 4B, see Figure 27. In the middle of this figure, the blackish particles found on non-polished powder surface are found, as also observed in Figures 24 and 25.

Figure 28 shows with arrows marked 1 a dark greyish area found next to porosity, which is also surrounded by blackish particles. Apart from these features, the matrix contains varying sizes of oblong formations, see especially upper right quadrant of the figure. The higher magnification image of the sample 4B in Figure 29 reveals the different sizes of the oblong precipitates; their length and width on the cross-section view varies between 2-25  $\mu\text{m}$  and 0.2-1  $\mu\text{m}$ , respectively. This shows their high geometrical aspect ratio of at least one order of magnitude.

According to SEM images, the sample 3A has the highest density of blackish particles on the surfaces whilst the rest are harder to separate regarding this feature. All these particles found in all samples were generally of the similar size of around 1-2  $\mu\text{m}$ . The dark greyish parts observed are of about the same sizes and shapes in all loose sintered samples as e.g. sample 2, but they were almost fully absent in the starch consolidated samples 3A and 4B. The oblong precipitates found with varying difficulty in all samples were all aligned mainly in three directions. The sizes of these were roughly two to three times larger in the samples 3A and 4B as compared to sample 2. The prior particle (powder) boundaries were, when sintered properly, often aligned with dark greyish areas as in sample 2, but for starch consolidated and sintered samples (3A and 4B) there were no prior particle boundary indication. All in all, the sintering appears to be more developed in the dense part than in the porous volume of loose sintered material (e.g. sample 2). As well, the same observation appears to hold for sample 3A compared to sample 4B.

#### 4.4.2 EDX

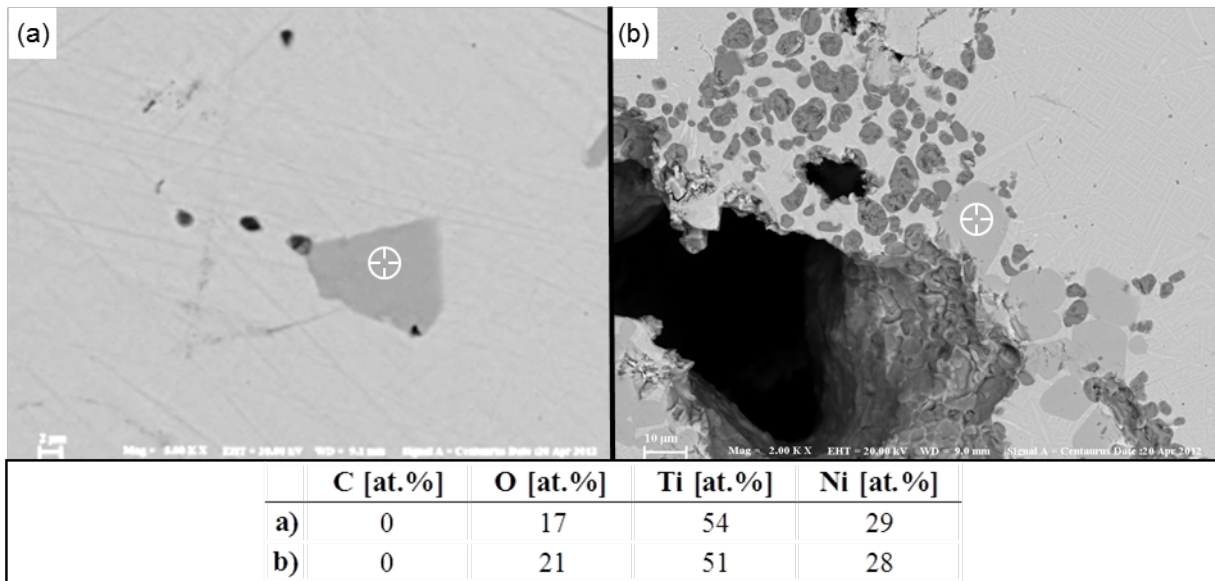


**Figure 30:** EDX spectrum points (crosshairs) and data for greyish area in a) sample 2, dense volume and b) sample 4B suggesting  $Ti_4Ni_2O$ .

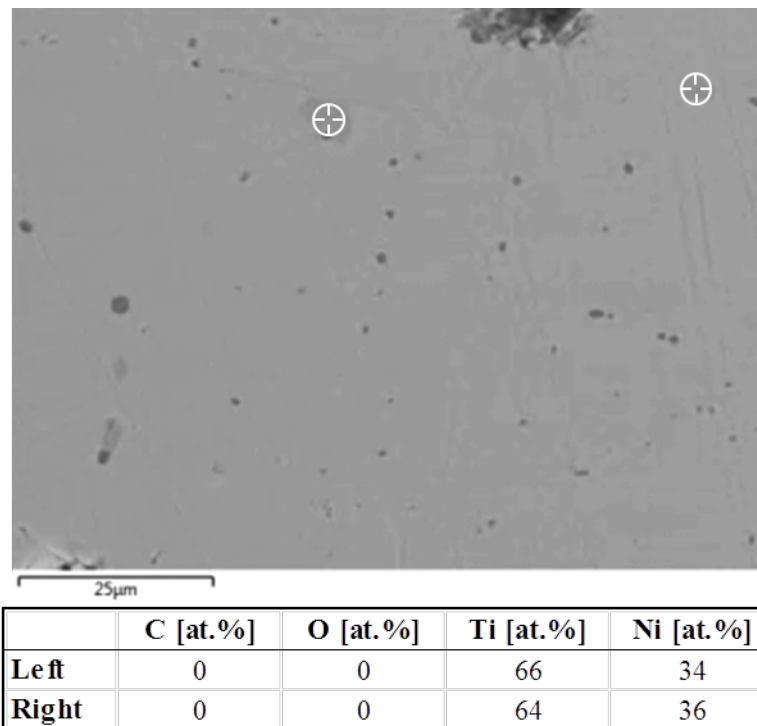


**Figure 31:** EDX evaluation points (crosshairs) and data on greyish areas in dense volume of sample 2 suggesting  $Ti_2Ni$ .

The EDX analyses of greyish features in dense sample 2 and 4B can be seen in Figure 30. The measured atomic compositions suggest that these features are composed mainly of the oxide  $Ti_4Ni_2O_x$ . However, contradicting to this, different atomic compositions were recorded for other greyish features in sample 2, see Figure 31, suggesting  $Ti_2Ni$  instead. It should, however, be noted that the phase  $Ti_4Ni_2O_x$  can have varying oxygen (O) content of  $0 < x < 1$  (Frenzel et al., 2010), which means that it is equivalent to  $Ti_2Ni$  when having no oxygen. Hence, it can be assumed that we are having the basically the same kind of precipitate, but with varying O-content depending on location.

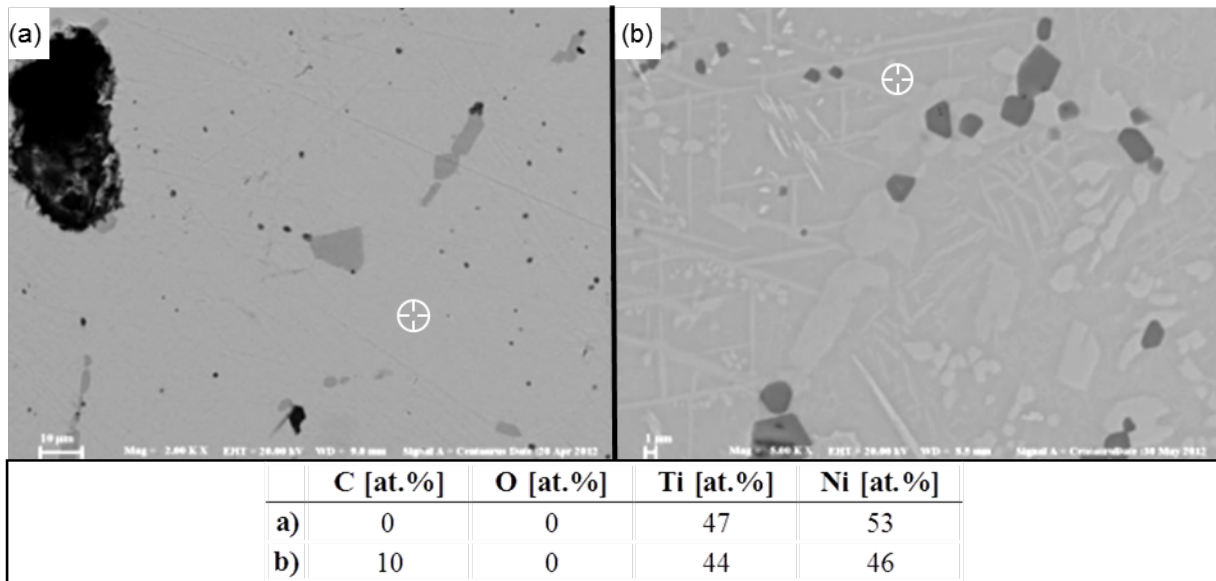


**Figure 32:** EDX spectrum points (crosshairs) and data for matrix area in a) sample 2, dense volume and b) sample 3B.

The overall EDX evaluation of typical data for the matrix is shown Figure 32. Regarding the phases of the matrix for loose sintered material sample 2 (see Fig. 32a), the atomic percentage distribution suggests NiTi or Ni<sub>4</sub>Ti<sub>3</sub>, or both together. For the the matrix of starch consolidated and sintered sample 3B, the EDX analyses (see Fig. 32b) suggest a blend of NiTi, Ni<sub>4</sub>Ti<sub>3</sub> and TiC. Hence, a main difference between the two kinds of processing seems to be the formation of TiC in the latter case.

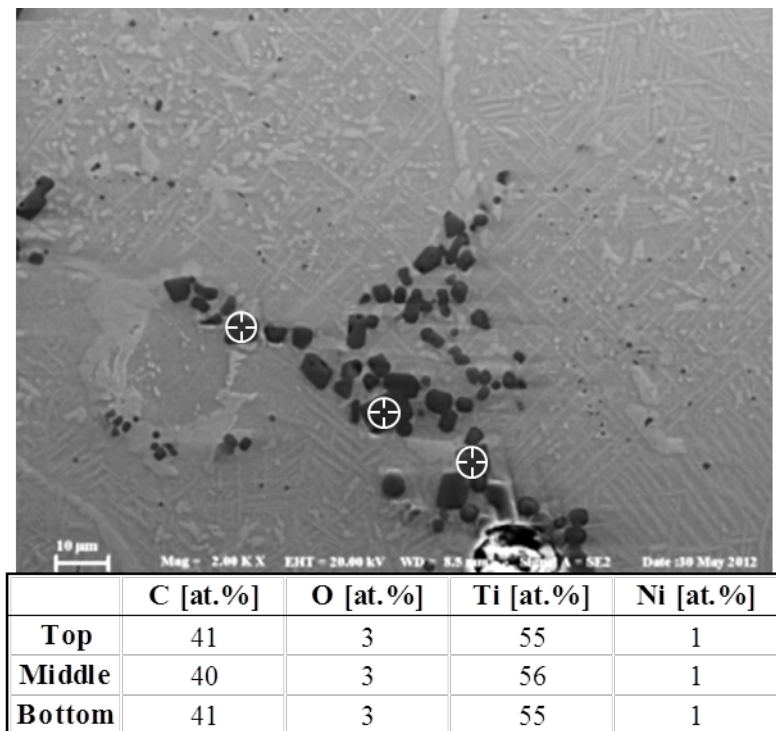


**Figure 33:** EDX evaluation points (crosshairs) and data from sample 3B.

The three EDX evaluation points and typical data of blackish particles can be viewed in Figure 33. The scan points are set on blackish particles that occur aligned along certain shapes or are present near prior particle boundaries in starch consolidated samples. EDX analyses show the blackish particles can be identified as mainly TiC. To what extent oxygen and nickel is contained in the particles remains to be clarified.

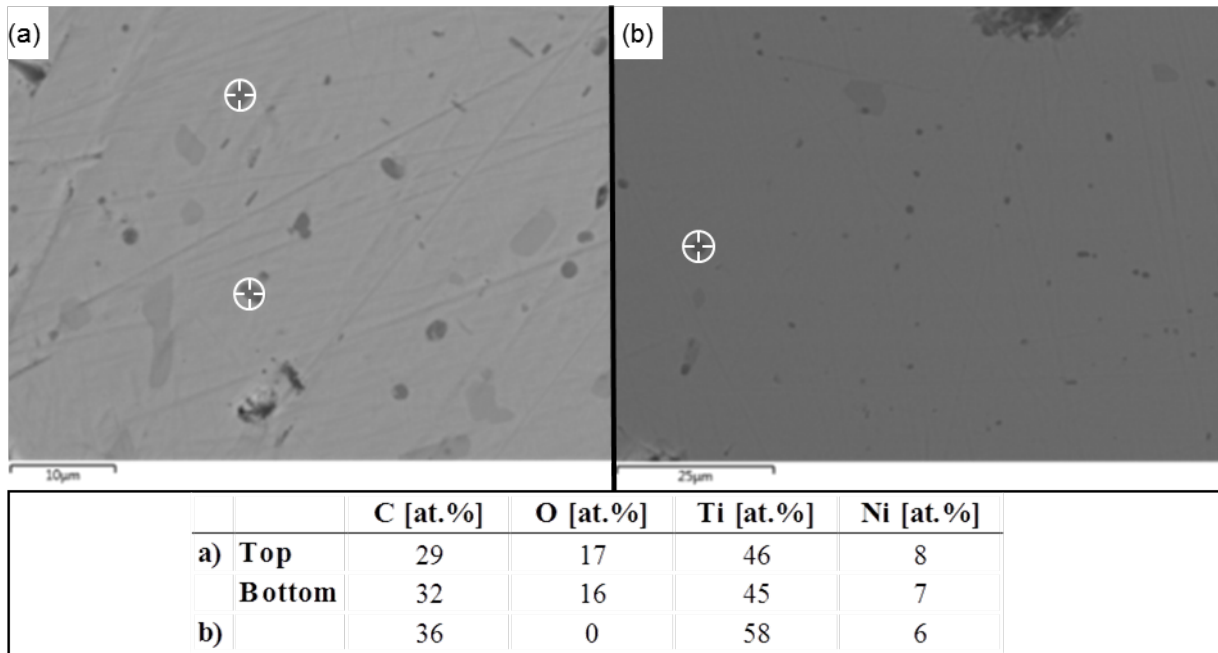


**Figure 34:** EDX evaluation points (crosshairs) and data on small blackish particles in dense volume of sample 2 of different areas (a and b).

Blackish particles that were smaller than in Figure 33 were found in sample 2, but the EDX analyses for these are not consistent as a can be seen from Figure 34a-b. Both figures illustrate particles of same size and shape, but the results of EDX analyses are different. Nickel and carbon content is of about the same level but oxygen is only found for particles shown in Figure 34a. A difference in titanium content is also shown between Figure 34a and b.

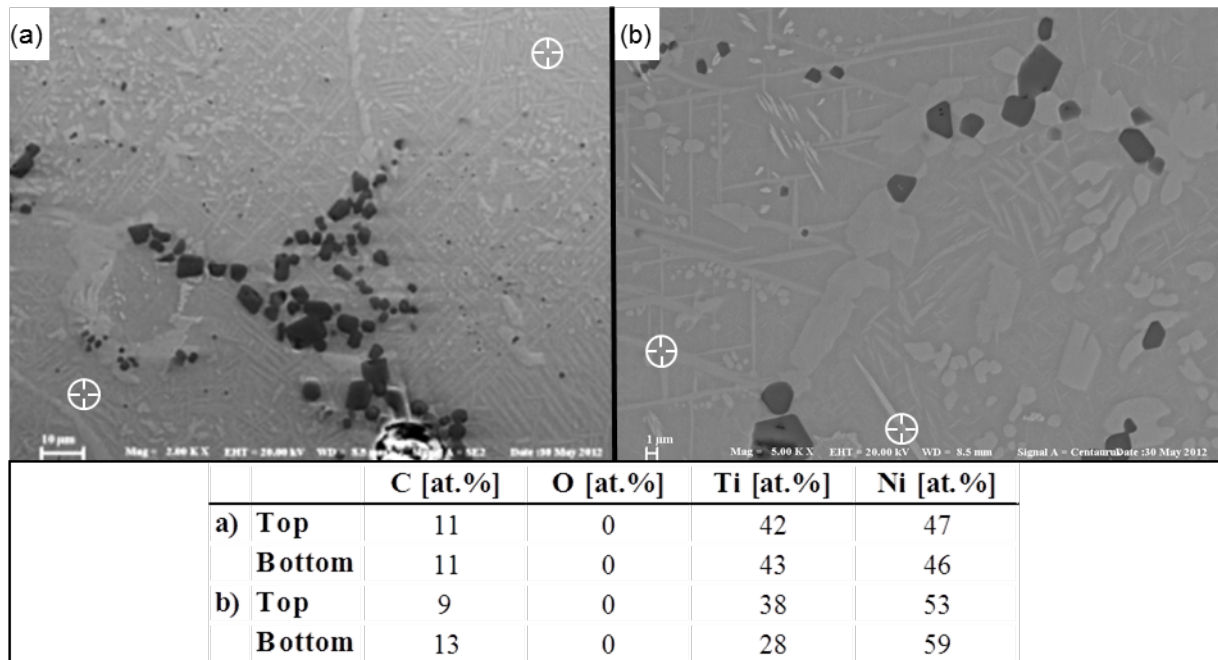


**Figure 35:** EDX evaluation points (crosshairs) and data on oblong formations at different areas of sample 3B.

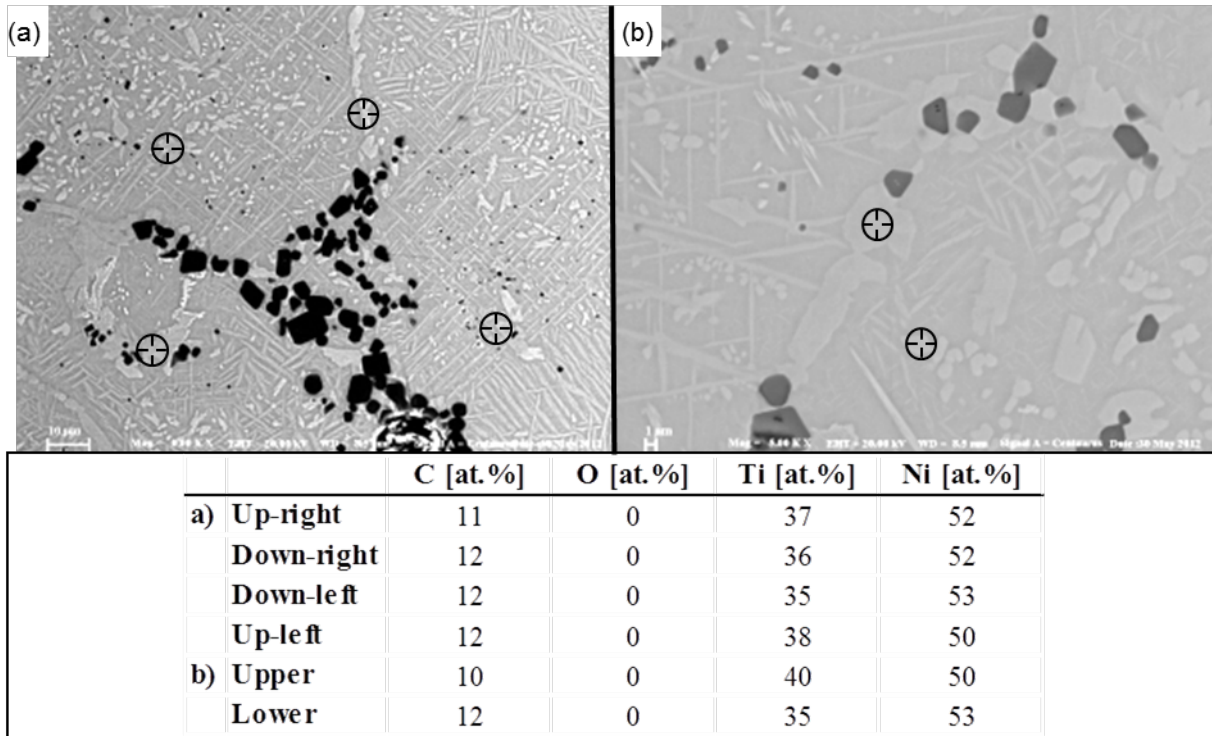


**Figure 36:** EDX evaluation points (crosshairs) and data on light greyish irregular shaped areas here in sample 3B of different areas (a and b).

Figure 35 shows EDX point analyses and typical data for sample 3B on oblong formations. Although all measurement points were set on wide oblong formations the data is not coherent. The data of the two different data points in Figure 35a match one another but not the data for b. Still, disregarding carbon (C), the average Ni/Ti ratio indicated by the analyses is about 1.3, which would suggest  $\text{Ni}_4\text{Ti}_3$ . Figure 36 shows EDX point analysis of irregularly shaped features of similar contrast as the oblong ones; the average Ni/Ti ratio found from these analyses is about 1.4.

#### 4.5 XRD

The XRD scans of powder, sample 2 (dense and porous volumes), 3A and 4B are shown in Appendix Figures 1-5. Two phases can be distinguished, they are NiTi (star) and  $\text{Ni}_4\text{Ti}_3$  (solid circle). They were both present in all scans and were distinguished with varying clarity. The presence of NiTi is of higher amount as compared to that of  $\text{Ni}_4\text{Ti}_3$  since the intensities of its characteristic peaks are higher. It can be observed that the three latter XRD scans (see Appendix Fig. 3-5) were a bit lower in intensity level compared to the first two (see Appendix Fig. 1 and 2). The peak notations of the two phases were therefore more hesitantly placed on the scan peaks of the last three. For clarity, the background has been removed from all scans.

## 4.6 Mechanical testing

In this subchapter the compression test data and the associated calculations are presented.

### 4.6.1 As-sintered test pieces

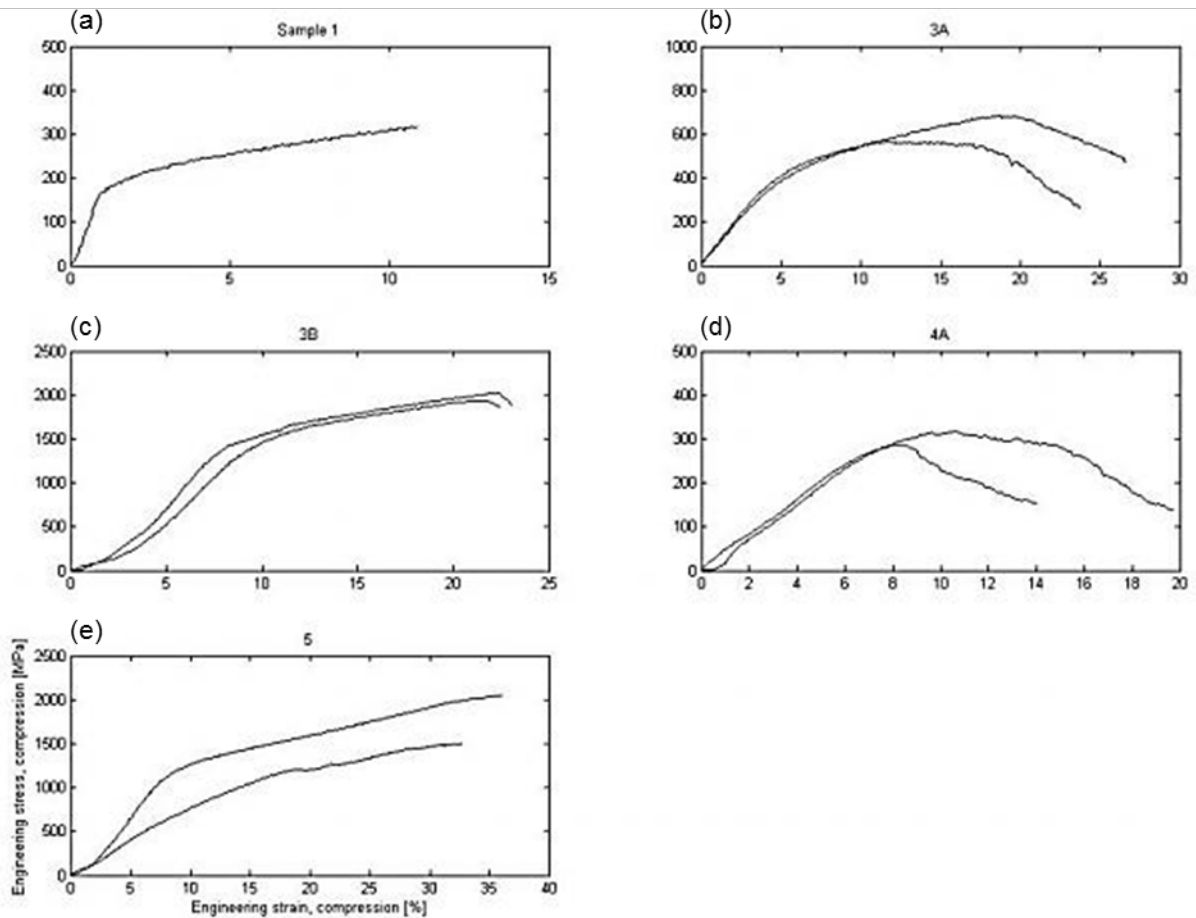


**Figure 37:** Engineering stress-strain ([MPa]-[%]) curves from compression tests data of the as-sintered test pieces from samples a) 1, b) 3A, c) 3B, d) 4A and e) 5.

The compression tests of test pieces from samples 2, 4B and 4C, see Appendix Figure 6, were discarded as they were considered failures and non-usable for further analysis of mechanical properties. The compression tests performed on test pieces from 1, 3A, 3B, 4A and 5 are presented in Figure 37. Disregarding absolute values, all samples but 4A have curves characterised by two linear portions. The sample data get more erratic as the strain builds up, an observation true for all curves. Also, in the beginning of the tests for 3B and one of two for 4A and 5 each there is a linear portion of the curve with a lower slope than the subsequent part. The subsequent larger slope linear portion of the curve is used for calculating E-modulus values shown in Table 6. Regarding apparent absolute values of offset engineering compression yield stress, engineering compression strength and engineering strain at fracture, the values derived from the tests can also be found in Table 6.

**Table 6:** The highest properties calculated from compression tests data of 1, 3A, 3B, 4A and 5.

	Sample				
	1	3A	3B	4A	5
$s_u$ [MPa]	315	685	2025	320	2045
E-modulus [GPa]	20	8.4	26	4.0	19
$s_y$ [MPa]*	175	370	1320	265	1070
$s_f$ [MPa]	315	480	1880	140	2045
$\epsilon_f$ [%]	10	27	23	20	36
*0.2 % offset					

Among the variants tested, samples 3B and 5 show the highest values for almost all properties. Regarding E-modulus, they are matched by sample 1 and regarding engineering strain at fracture ( $\epsilon_f$ ) by 3A and 4A. The fact that samples 3B and 5 show best properties is, of course, the lower porosity levels (7% and 12%) compared to those of the other samples (<20-30%). Furthermore, the non-homogeneous character of the porosity also means uncertainty in the measured values. Still, as can be seen from Table 6, when sintered properly as e.g. samples 3 and 5, compression strength values of around 2000 MPa combined with low modulus of around 20 GPa can be obtained.

#### 4.6.2 Anisotropy

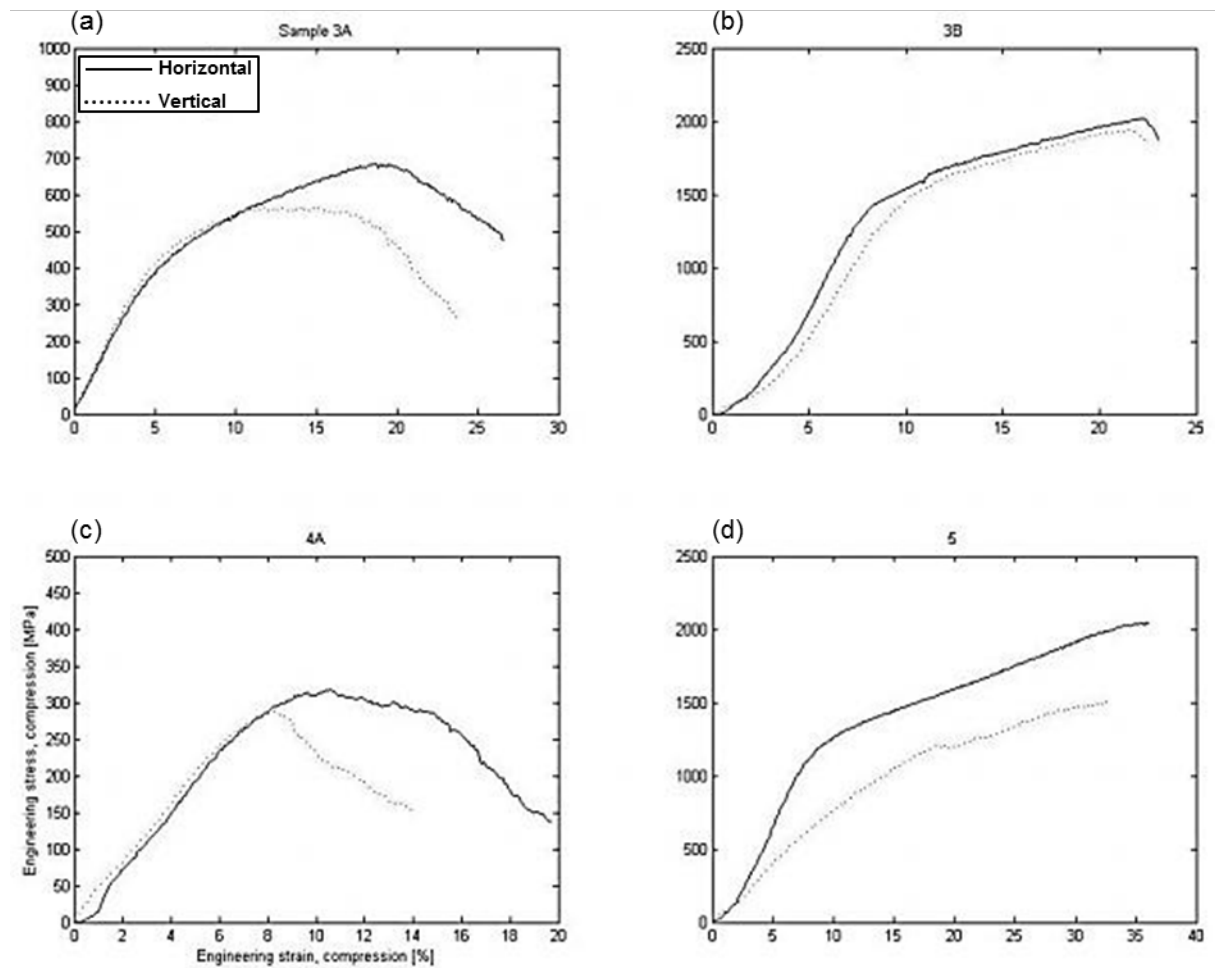


**Figure 38:** Engineering stress-strain ([MPa]-[%]) curves of the compression tests data generated from test pieces of samples a) 3A, b) 3B, c) 4A and d) 5 divided into horizontal and vertical EDM extraction setup of respective sample.

The compression tests of test pieces from samples 3A, 3B, 4A and 5 divided into horizontal and vertical wire EDM cut samples (c.f. Fig. 12 for illustration of preparation) can be seen in Figure 38. Whether the test piece is horizontal or vertical makes less difference in sample 3B. On the other hand, test pieces from 3A and 4A, do not differ until a certain part of the test has been performed while for sample 5 the differentiation begins more closely at the start of the compression test. Comparing horizontal and vertical test pieces, the test pieces from sample 3B and 4A are not differing in stress and strain upon failure as they fail at the same stress level. In the other two samples, the vertical test pieces fail at both lower stress and lower strain levels.

**4.6.3 Heat-treated test pieces**

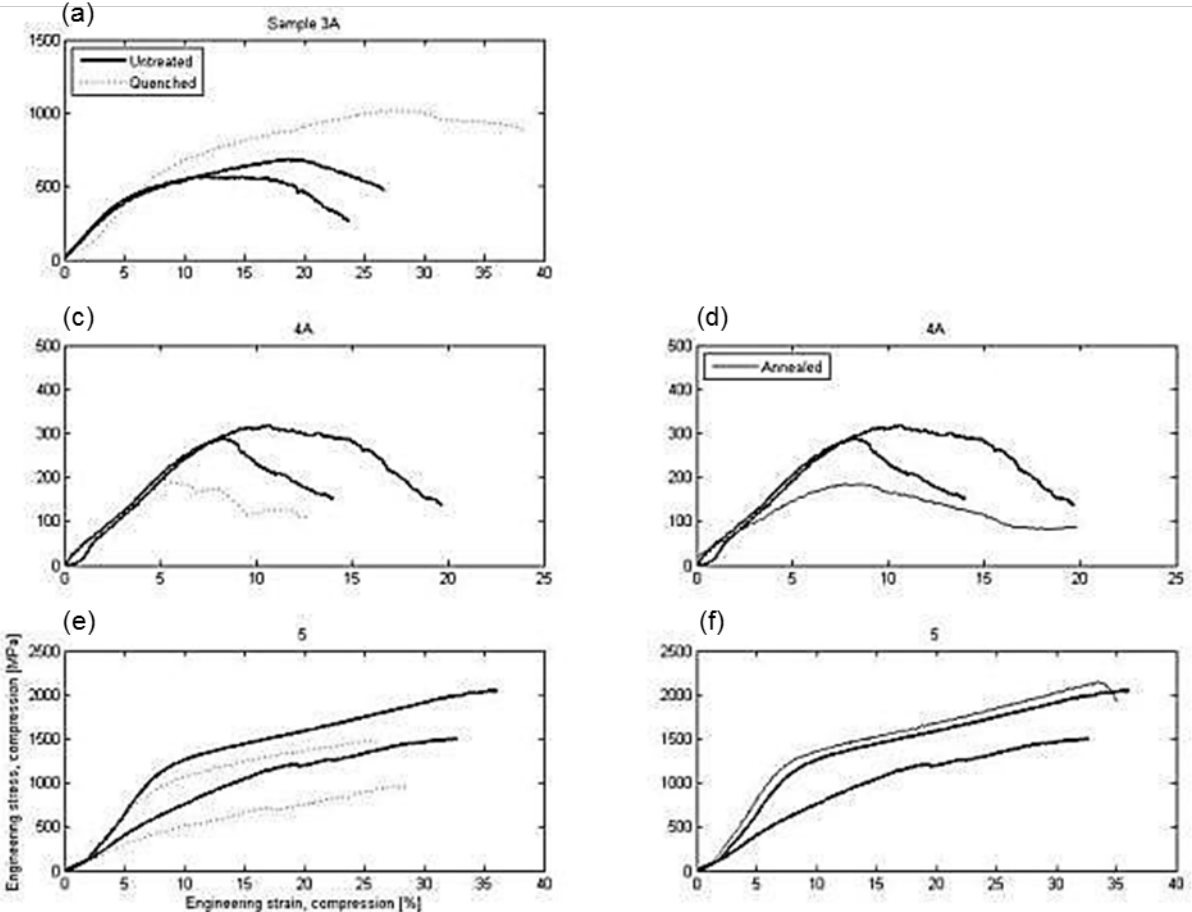


**Figure 39:** Engineering stress-strain ([MPa]-[%]) curves from compression tests data of test pieces from samples a) 3A, c) and d) 4A, e) and f) 5 with respect to untreated, quenched and annealed test pieces. The 3A sample did not generate enough test pieces to enable an annealing and testing.

The engineering stress-strain curves for untreated, quenched and annealed test pieces from samples 3A, 4A and 5 are presented in Figure 39. Regarding quenched test pieces (a, c, e), they generate a curve following the untreated one in the first part to then diverge upwards for sample 3A and downwards for 4A and 5. The quenched test pieces of samples 4A and 5 both fracture at a lower stress and strain levels than the untreated, which is opposite of what happens for test pieces from sample 3A. An observation for the 3A test pieces is that the quenched test piece curve looks like a scaled up version of the higher one of the two untreated test piece curves. Another observation is that the

quenched test piece curves of sample 5 look like scaled down versions of the untreated test piece curves.

The annealed test pieces (d and f), diverge from the untreated almost immediately after test start, to diverge downwards and upwards for the test pieces of sample 4A. However, the annealed test piece curves diverge less than the quenched regarding stress and strain upon fracture. Additionally, the annealed test piece curve of sample 5 follows the untreated one almost identically with a stress increased shift created already at <2% strain. Hence, the effect of heat-treating the sintered samples is not consistent.

#### 4.6.4 Cyclic tests

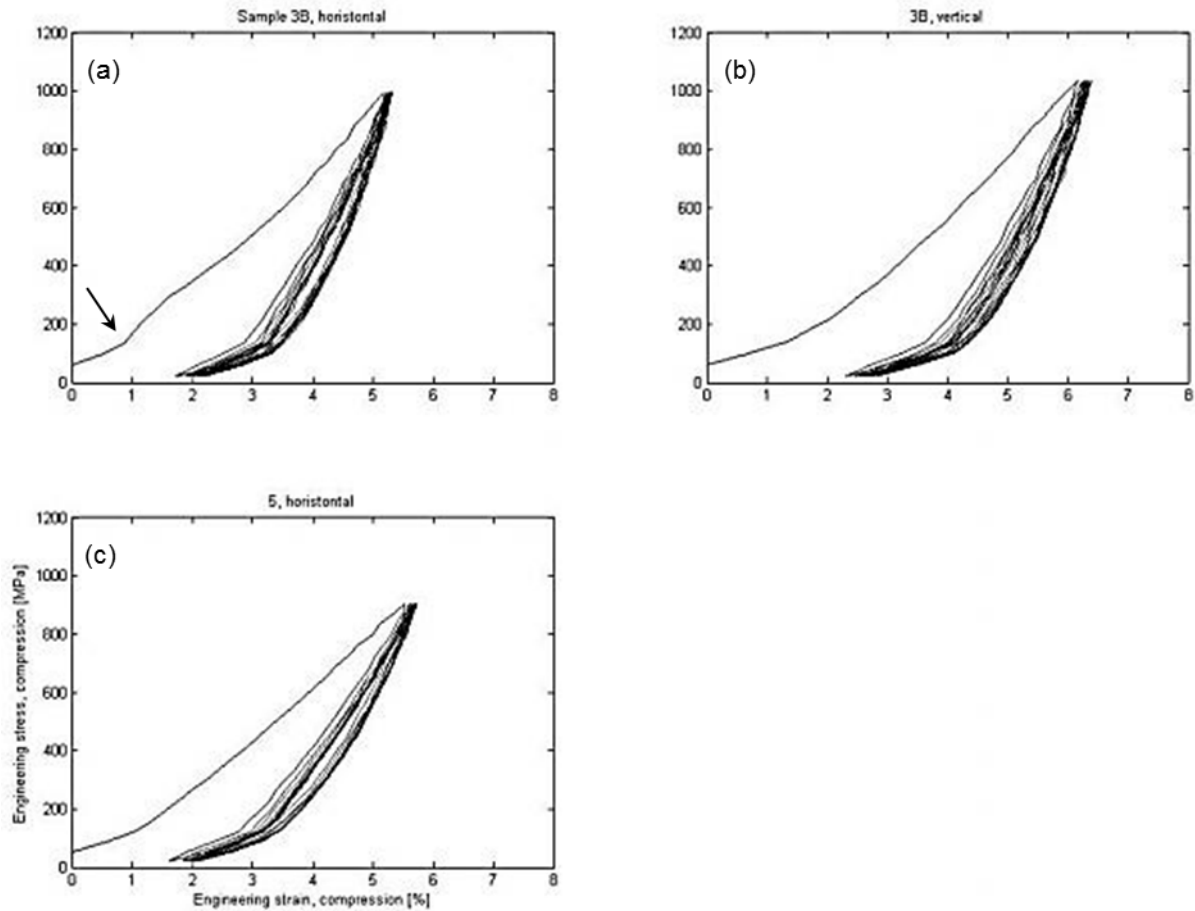


**Figure 40:** Engineering stress-strain ([MPa]-[%]) curves from the 10 cycles compression test data of the test pieces from samples a) and b) 3B (one horizontal with curve knee denoted (arrow), one vertical) and c) 5 (one horizontal).

The cyclic compression tests of test pieces from sample 3B (one vertical, one horizontal) and sample 5 (horizontal) are presented in Figure 40. Since the maximum force applied on the test pieces from sample 3B is a bit higher (5.5 kN) than for the sample 5 (5 kN), the maximum pressure is also a bit higher for sample 3B. In all curves, increased residual strain can be seen as the ten cycles are performed and the maximum residual strain is generated on the last cycle. Also all cycles 2 to 10 follow the first loading line fairly well, with the difference of a shift towards higher strain upon decreasing stress (unloading). This shift is most clear above the knee denoted with an arrow (see Fig. 40a) as the curves below that are relatively unchanged upon loading for all cycles. Comparing 3B horizontal and vertical test pieces, the vertical test piece (see Fig. 40b) experiences higher maximum and residual strains and with almost identical stress. In Table 5 the residual strains after compression

tests and after annealing are presented. The recovery of all test pieces after annealing lies between 40 and 60%, with a difference between the horizontal and vertical test pieces of 55 vs. 43%.

**Table 7:** Residual strains from cyclic compression, before and after annealing. Both horizontally (h) and vertically (v) extracted samples were tested.

Residual strain	Samples		
	3B (h)	3B (v)	5 (h)
Before anneal [%]	2.1	3.1	2.9
After anneal [%]	1.0	1.8	1.4
Recovery [%]	55	43	50

## 5. DISCUSSION

This chapter aims to interpret and explain the results generated in this report.

### 5.1 Sample production

Samples were initially prepared by means of loose powder sintering. An inherent problem with loose powder sintering is that any lack of proper powder packing results in less good densification during the sintering. The differences in sintering within the loose powder sintered samples (samples 1 and 2) can in this respect be explained by several factors. The higher surface densification (shiny surface) can be explained partly by the crucible geometry. The denser volume is formed by the heat from the crucibles as they are solid and static as opposed to the flow of argon above them and the powder surface during sintering. This causes the temperature to be higher closer to the crucible, improving the sintering. Another factor is that if local differences in composition lead to conditions for low enough melting temperature, liquid will run downwards with gravity inside the crucible. According to the previous assumption regarding crucible effect chances of this are higher closer to the crucible wall. In addition, the pouring of the powder into the crucible before sintering can also form differences in packing density inside the crucible. The difference between sample 1 and 2 (see Fig. 13a and b) can be explained by the use of different crucibles. The sample 1 was sintered in a simpler heat-resistant and more porous ceramic crucible, whilst the sample 2 was sintered in a denser alumina ( $\text{Al}_2\text{O}_3$ ) crucible. The alumina crucible can be considered keeping the heat better than the other due to its low or non-existing porosity. The issues mentioned can be of importance from a material design point-of-view. The uneven sintering across the powder volume might be avoided by adjusting the temperature and heating rate to create conditions at which the denser structure cannot form at crucible wall. Another way to achieve a more homogeneous density in loose powder sintering can be to use more porous crucibles; the sample made in such (see Fig. 13a) showed lesser amount of more densified structure at the crucible wall (see Fig. 13c for general illustration). Furthermore, the layered structure (c.f. Fig. 13a) might be avoided by adjusting the way to transfer and place powder into the crucible. Frequent tapping and pouring little by little or pouring all at once carefully are ways of better controlling the powder filling.

In order to improve the particle packing and allow possible manufacture of shaped specimens, so-called starch consolidation was then employed to fabricate green body samples for sintering. The experiments can be considered as screening tests at this stage. Different starch consolidation parameters such as powder load, dispenser level, dwell time and starch content were varied. Appropriate disc-shaped specimens were fabricated, while process optimisation was outside the scope of the current study. With the starch consolidation, an added complexity is introduced as processing constituents are left in the shaped specimen and need to be removed during heating up before the high temperature sintering. The obtained rugged surfaces of sintered starch consolidated samples can be explained by the incineration of the additives used during starch consolidation. Apart from starch, the anti-foaming agent, the dispersion agent and the thickener also are organic, i.e. carbon-based compounds. As the sintering atmosphere is composed of argon (i.e. no oxygen), these carbon-based products carbonise instead of burn up into water and carbon dioxide as in conventional combustion. This means formation of soot (carbon) on the surfaces of starch consolidated samples during the heating cycle of the sintering process.

The rugged surface of starch consolidated samples can easily be removed with polishing. However, the surface created in the open porosity inside the sample is another matter. Chemicals of certain type could remove the residual carbon but as has been tested the residuals does not come out. The starch

consolidated and sintered samples were subjected to ultrasonic cleansing in acetone for 5 min and no residuals were released.

Mainly, three different geometrical changes were observed after sintering. First, the concave form of the final samples is due to thermal shrinkage and geometrical restrictions upon cooling. The material in the middle cannot shrink in any other direction than towards the middle but the side material can shrink in all directions but outwards radially. Also, the cooling effect from the flowing argon gas will cool the sides faster than the middle as the bottom is protected by the plate at which it was placed on. Second, the broadened base of e.g. sample 4B can be explained by its higher powder content making it settle towards the plate. Third, cavities can occur (see Fig. 14) caused by accumulation of additives that upon sintering carbonise and leave such locations.

The shape changes occurring during sintering can be counteracted by designing the process. For example, a disc-shaped green body with convex top and top-heavy geometry may show a flat top and vertical sides after sintering. The cavities illustrated in Figure 14 can be removed by improving mechanical mixing in the starch consolidation process.

## 5.2 Microstructure

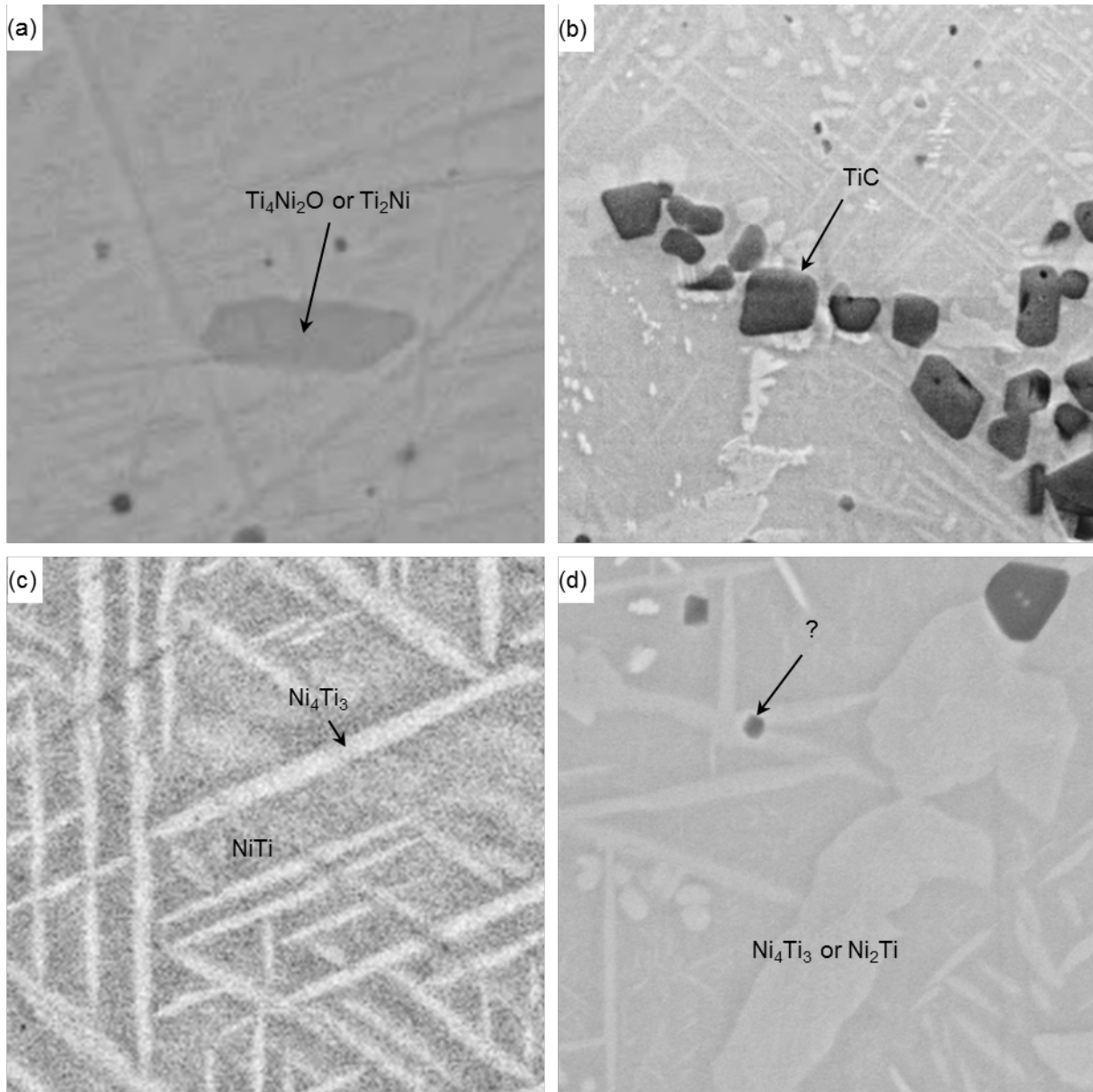


**Figure 41:** a) The greyish area of  $Ti_4Ni_2O$  or  $Ti_2Ni$  in horizontal length of around  $8\ \mu m$  here in sample 2. b) The bigger blackish particles here in the starch consolidated sample 3B composed of  $TiC$ . The marked particle is around  $6\ \mu m$  in its longest direction. c) Oblong formations of  $Ni_4Ti_3$  and main matrix of  $NiTi$ , denoted by arrows, here in sample 4B with marked oblong formation length of around  $10\ \mu m$ . d) The undefined small blackish particles (arrow, diameter around  $1\ \mu m$ ) and irregular shaped formations of  $Ni_4Ti_3$  or  $Ni_2Ti$  here in sample 3B.

Microstructure control is essential when processing  $NiTi$  material to arrive at properties such as superelasticity or shape memory effect. Basically, preserving as high amount as possible of the  $NiTi$  phase is a key issue in this respect. From the results of this thesis it is clear that neither loose powder sintering nor sintering of starch consolidated material gave monolithic  $NiTi$  structure. Figure 41 illustrates a summary for both kinds of sintered variants. Besides the matrix  $NiTi$  phase, greyish areas were observed in both cases and confirmed to be  $Ti_4Ni_2O$  or  $Ti_2Ni$  (see Fig. 41a). The formula of the former phase can be expressed as  $Ti_4Ni_2O_x$  with  $x$  ranging  $0 \leq x \leq 1$  and, hence, it transforms to  $Ti_2Ni$  when having no access to oxygen. Thus, depending on local availability of oxygen it seems reasonable that

both phases occur. Their similarity is supported by Mueller and Knott, who found that  $Ti_4Ni_2O$  and  $Ti_2Ni$  have almost the same structure (Mueller & Knott, 1963).

In sintered starch consolidated material, TiC particles are also found (see Fig. 41b), frequently located at pores or prior particle boundaries. It is suggested that their presence originates from the reaction between titanium and the carbon coming from the additives of starch consolidation. This suggestion can be further based on the fact that the additives are the only carbon-containing substances used for starch consolidation.

For both kinds of sintered samples, secondary precipitation also occurs. Figure 41c shows the lenticular shaped  $Ni_4Ti_3$  and the matrix NiTi phases. The former can be said to be of lenticular shape as opposed to needle like as if that was the case; almost round precipitates would be visible for needles positioned to come out of the surface in direction of its normal. Such almost round precipitates were not visible. Also, the lenticular shape assumption is supported by the study of Koskimaki & Marcinkowski in 1969, who stated that  $Ni_4Ti_3$  appear in lenticular shape in NiTi. Both the  $Ni_4Ti_3$  and the NiTi phases were also confirmed in the present study according to XRD analysis.

In Figure 41d, the smaller blackish features discovered in all samples are shown (arrow). They were of more circular shape than the TiC particles and were seldom larger than 1  $\mu m$ . They can also be seen around the greyish feature in Figure 41a. As their size limits their analysis in both XRD and EDX their composition is outside the scope of this thesis. However, observations resembling this have been seen by Ismail et al. in 2011, who considered them to micro-pores due to Kirkendall effect. This is an effect based on diffusion of atoms with different intrinsic diffusion coefficient in the given matrix. As they move, one kind does so more effortlessly than the other, causing voids or pores to form. Nickel has ten times higher intrinsic diffusion coefficient than titanium making this effect possible (Divinski et al., 2009).

Figure 41d also shows the irregular shaped features often seen on prior particle and/or grain boundaries. Disregarding carbon, the EDX analyses suggested  $Ni_4Ti_3$  or  $Ni_2Ti$  which is also indicated in the figure.

As all above phases except NiTi and  $Ni_4Ti_3$  are holding only fractions of the sample volumes, the XRD analysis cannot be used to discover them. Also, deconvolution of the XRD data was not available, and since many of the actual phases have coinciding XRD peaks, see Appendix Table 1, this is necessary to gain more information from the XRD.

### 5.3 Porosity and shrinkage

Considering the loose powder sintering, the higher porosity of sample 2 as compared to sample 1 (c.f. Table 4), can partly be explained by that the latter was removed from the argon atmosphere at higher temperature of up to 300°C (see Table 2). This could have caused the powder to oxidize more taking up volume which would otherwise be porosity (Firstov et al., 2002). Also, sample 1 was sintered in slightly less pure argon gas. Let us now consider the sintered starch consolidated samples. First, although everything other than sample position in the furnace was identical for samples 3A and 3B the porosity was almost four times higher for sample 3A. Sample 3A was placed closer to the argon gas nozzle making it cool off more when sintering causing it to keep the porosity at a higher level. The same reasoning can be applied to the porosity value of sample 5. This sample was sintered with an obstacle lying next to it, hindering it from gaining all the cooling effect of the argon gas flow, in an attempt to mimic previous sintering trials.

The above reasoning cannot be applied for samples 4A-C as the positioning of these inside the furnace was not recorded. Since the positioning could cause porosity differences of almost four times and the differences in porosity for samples 4A-C is low, a further reasoning around these samples' porosities is left out. This would be highly speculative and not in accordance with science practice.

A comparison between porosities of sample 3B and 5 is however more meaningful. The higher porosity of sample 5 can be explained by the shorter dwell time of 40 min instead of 100 min. The shorter time gives less time for diffusion and to eradicate powder particle surfaces causing it to keep a higher porosity upon sintering.

The measurements of porosity performed based on sample geometry and weight do not enable highest accuracy or distinguishing between open and closed porosity. Archimedes principle measurements of weighing and submerging samples in water, with and without paraffin wax in the pores to calculate open and closed porosity would be a more accurate method. But with the small test pieces at hand, this was not possible to perform with desired accuracy.

Apart from the above mentioned possible errors, the theoretical density taken for pure NiTi as the density for fully dense material is not fully true as can be seen from the SEM investigations (c.f. subch.4.4). There is above all, a mentionable amount of  $\text{Ni}_4\text{Ti}_3$ , the density of which is  $6790 \text{ kg/m}^3$  (Saburi et al., 1986) is higher than the density of NiTi ( $6450 \text{ kg/m}^3$ ), possibly causing the porosity measurements to be overestimations according to Equation 1.

## 5.4 Mechanical properties

The sintering of packed loose powder and starch consolidated samples led to different mechanical properties, one reason being different final microstructures. For example, the average of 22% higher hardness of the latter samples can be explained by the higher amount and size of  $\text{Ni}_4\text{Ti}_3$  precipitates in the sintered starch consolidated samples. Although TiC was also present in the sintered starch consolidated material, it appeared on prior particle boundaries and on pore surfaces and should have no practical influence on the microhardness level, considering also that testing was applied away from the pores.

To find out the tentative strength levels and possible superelasticity of the sintered materials, compression tests were performed. The compression tests performed on samples 2, 4B and 4C were here discarded for further analysis as they were considered not representative of the material, see Appendix Figure 6. Instead they represented different reasons for inadequate properties such as uneven pore distribution. Too large agglomeration of pores implies that the solid material that is left has to carry all load of the sample cross-section, meaning high pressure even at low forces. Other reasons for inadequate behaviour can be cracks and small necking due to incomplete sintering. For samples 4B and 4C there were several test pieces all interpreted as defective as above. A probable reason is that the higher powder load of sample 4B and less amount of dispersion agent of sample 4C caused settling and agglomeration of powder, respectively. This could have created inhomogeneous powder packing as explained before. The compression tests of samples 1, 3A, 3B, 4A and 5 were however possible to perform successfully (c.f. Fig. 37). Arguably, in loose powder sintered and starch consolidated tests, the first part of the curve should be regarded with criticism. This is a fact as these stresses correspond to the compression of the machine during the test, before it has good contact with the sample. Another alternative is that it is due to the test pieces not being perfectly parallel. However, even removing the first part would not change the overall interpretation from the shape of the curves. Additionally, the plastic strain that a material can withstand in compression will of course be different than that it can experience in tension since necking and plastic instability is not possible. Therefore,

the plastic strains indicated in the tests performed cannot be compared directly with data from tensile testing. However, even if viewed as indicative values, they demonstrate a possible extent of deformation before onset of collapse of the sintered NiTi structures. Barrelling was also observed, but as the samples were fully fractured a correction for this was not available. Therefore only general comparative notes and E-moduli are treated in the discussion below. The other data of Table 4 can be used as comparative data for future studies instead.

The compression tests of samples 1, 3A and 4A (see Fig. 37a, b and d) gave all lower values than for 3B and 5 (c and e). This can be explained by higher porosity and other reasons for failure such as incomplete sintering and too large agglomerations of pores (German, 1994). The difference would decrease if porosity was taken into consideration but this has not been made due to the lack of accuracy in the porosity calculations.

The higher yield strength values of test pieces 3B and 5 in compression can be explained by the  $\text{Ni}_4\text{Ti}_3$  precipitates in the samples which have been proven by Miyazaki et al. in 1982 to alter its mechanical properties. They precipitate harden the material and delays yielding upon stress increase. The E-modulus compared to theoretical level for NiTi can be explained by the porosity levels (7.0 and 12% respectively). Above all, the literature values of Table 1 are from tensile testing and a direct comparison to them is not recommendable since the situation of testing is different as addressed above. Still, for the best sintered samples (samples 3B and 5), compression strength of around 2000 MPa was achieved, the possible drawback being the extent of superelasticity due to the secondary phase precipitation (see further below).

The possible anisotropy in properties was tested by compression testing of specimens taken from sintered samples in vertical and horizontal directions. The curves of vertically extracted test pieces showed generally lower pressure values but as the differences were very small and the samples were few more general statements should be avoided.

Since it is of crucial importance to have appropriate microstructure, compression tests were carried out for certain samples in both as-sintered and heat-treated conditions in quenched or annealed states. No specific trends with respect to general effect of the heat-treatments could be found. Instead, differences between un-treated, quenched and annealed conditions were specific for different variants of samples. Regarding quenched samples, the untreated showed higher values in compression tests for samples 4A and 5 but lower for sample 3A. The same reasoning can be applied to annealed test-pieces of sample 4A and 5 as the former showed higher values, while lower for the latter. An explanation for this can be that the samples already are mainly in B2 phase (NiTi). The effects sought for by quenching, i.e. forming martensitic phase, is then avoided when the temperature of the quenched pieces reach ambient temperatures again. At such temperatures the  $A_f$  might have been passed upon warming, causing the sample to retransform into B2 phase. The effects sought for by annealing are then also absent as no transformation temperature lies in the region between ambient and annealing temperature.

Cyclic compression tests were also performed, this to depict the superelastic behaviour. Considering the engineering stress-strain curves in Figure 40, it should be noted that the measurements below the knee (arrow) are believed to exist due to compression test machine movement or test piece being non-parallel, as mentioned above. The residual strains after compression, see Table 7, differed between 2 and 3%, most probably because all test pieces are unique and previously mentioned defects can occur in varying amounts. Still, after annealing the shape memory recovery level was around 50% (43, 50 and 55%). Hence, regarding these samples one can state that there is a more unified shape memory effect (SME) property present.

All in all, the precipitates of  $\text{Ni}_4\text{Ti}_3$  have increased the hardness and yield strength while porosity has decreased the E-modulus compared to fully dense monolithic NiTi. Furthermore, no general trend was seen supporting anisotropy, but as mentioned above chances of its existence are possible since the starch consolidation implies working with fluids which could result in varying powder packing in different directions due to e.g. settling. Neither was there a general trend for untreated, quenched and annealed test pieces. Most probably this is because the phase constitution of the as-sintered (untreated) stage is recovered upon warming to room temperature after quenching and unchanged upon annealing and cooling. Regarding superelasticity and SME the former was not tested properly as there was not full direct recovery upon unloading in the cyclic tests. That would have enabled an increase in maximum test stress and a control if the P-shaped curve of Figure 3 was possible to generate with the material. Considering SME, it was tested through heating the cycled test pieces and measuring the recovery and 50% and not 100% recovery was achieved. Tests by Asai, 1982 have shown that precipitates of  $\text{Ni}_4\text{Ti}_3$  enable the best super-elasticity and SME properties when they are small and present in high volume fraction. In the starch consolidated samples of this thesis, the  $\text{Ni}_4\text{Ti}_3$  precipitates were large and of high density (high volume fraction), but small and of low density (low volume fraction) in the loose powder sintered samples. Arguably the forming of TiC creates a lower concentration of titanium in the matrix which benefits the formation of  $\text{Ni}_4\text{Ti}_3$ . This is a phase which uses less titanium atoms than nickel atoms upon formation. Clearly, there is space for further optimisation.

## **5.5 Biocompatibility considerations**

No tests for biocompatibility were performed on the manufactured samples, but the existence of pure nickel on its own is proven almost non-existing as none of the XRD scans show the presence of it in pure condition. Instead, nickel is always bonded to titanium in either NiTi or  $\text{Ni}_4\text{Ti}_3$ , from which nickel is very difficult to be released. The surfaces showed presence of TiC, which is a ceramic. Ceramic coatings, with their excellent corrosion and wear resistances, high hardness and good biocompatibility, are often used to modify the surfaces of artificial devices (Sonoda et al., 2004), and the presence of it should therefore be of no direct impact. According to the ultrasonic cleaning performed on the sintered samples, this revealed that the residues were not released from the pores in the sintered samples. If this means that significant amounts of residues are present remains to be proven. If this was the case an unwanted and uncontrolled deposition of particles would most probably be present when in use in the human body.



## 6. CONCLUSIONS

From this study, the conclusions are as follows:

- Pre-alloyed NiTi powder can successfully be synthesized into bulk porous samples by argon sintering of starch consolidated material. The porosity is possible to tune and by optimizing the sintering parameters the desired microstructure can be achieved to enable shape memory effect and superelastic properties.
- The starch consolidation technique can be advantageous to freely obtain the desired shape and form of the sintered porous material.
- Apart from the sintering cycle of time and temperature, the results of loose powder sintered samples are mainly affected by the choice of crucible, the argon gas flow and the method of placing the powder in the crucible.
- No elemental nickel is detectable by XRD in the samples after sintering of pre-alloyed NiTi powder which is beneficial for biocompatibility.
- The porosity of starch consolidated samples after sintering is highly dependent on the flow and movement of the argon gas within the furnace. The more cooling effect allowed to be implemented by the gas, the higher is the porosity.
- After sintering, starch consolidated samples have about 20% higher hardness than loose powder sintered samples. The reason for this is that the starch consolidated samples form thick and long  $\text{Ni}_4\text{Ti}_3$  precipitates in higher volume fraction while loose powder sintered samples form thin and short  $\text{Ni}_4\text{Ti}_3$  precipitates in lower volume fraction.
- Starch consolidated samples can be sintered into a mainly open porosity structure material (about 7-12% porosity) that in compression tests show a yield stress above 1000 MPa (or even up to 2000 MPa) and an E-modulus of around 20 GPa. The yield stress is higher than for monolithic NiTi (B2 phase) mainly because of high amounts of the  $\text{Ni}_4\text{Ti}_3$  precipitates. The E-modulus is lower than for dense NiTi (B2 phase) mainly due to porosity.
- The starch consolidated samples exhibit a shape memory recovery of above 50% after cyclic loading.



## 7. FUTURE WORK

In this chapter of future work some suggestions of how to continue the study of loose powder sintered and sintered starch consolidated samples are stated.

- With the aim of using porous NiTi from sintered starch consolidated samples as a biomaterial biocompatibility tests are needed. Extensive tests on the biocompatibility of conventionally fabricated NiTi have already been made (Ryhanen et al., 1998) but whether the additives used in starch consolidation form undesired features, substances, etc. is yet to be investigated.
- In order to fully determine the phases formed during sintering of pre-alloyed NiTi powder more investigation is needed. The first and simpler step would be to enable use of deconvolution of the XRD scans and get more information thereby. The next and more extensive step would be to use X-ray photoelectron spectroscopy (XPS) to characterize the surfaces of the sintered powder particles and fracture surfaces.
- Detailed investigation can be performed on how the sintered samples are affected by the many parameters of starch consolidation and its sintering. An evaluation of each parameter and its effect on the sintered sample is an extensive project, but it would generate the experience of starch consolidation with subsequent sintering to broaden its use. Some parameters are: pre-hold time and temperature, dwell time and temperature, cooling alternatives, sintering atmosphere, starch contents, dispersion agent content, powder load, thickener content, sample size and shape, etc.
- Regarding mechanical properties several test pieces from each sample need to be generating the same data in compression testing. This is required to draw more general conclusions. Subsequently, compression tests and heating allowing the superelasticity and shape memory effect to be evaluated are important. Also, fractography of mechanically tested sample surfaces could generate information about plastic deformation and fracture morphology which is useful for further studies.
- Regarding the thermomechanical properties of the sintered samples, an investigation of the transformation temperatures and their dependence on production parameters is needed. This can be achieved by Differential scanning calorimetry (DSC). Detailed DSC investigations can be useful for understanding thermal characterization and kinetics of the shape memory alloys.



## 8. REFERENCES

- Asai M, Graduation Thesis, University of Tsukuba, 1982.
- ASM Desk Editions > Metals handbook > Special-purpose materials > Shape memory alloys > Commercial SMA Alloys, accessed 2012-05-24, Chalmers University of Technology license (e-book).
- Bansiddhi A, Sargeant TD, Stupp SI, Dunand DC, “*Porous NiTi for bone implants: A review*”, *Acta Biomaterialia* 4, pp 773-782, 2008.
- Bellen P et al., “*Thermodynamic assessment of the Ni-Ti phase diagram*”, *Materials Research and advanced Technologies*, 1996 with use of “*Thermo-Calc Software*”, Thermo-Calc Software AB, Chalmers University of Technology license, Version July 1st 2010.
- Buehler WJ and Wiley RC, “*The properties of TiNi and associated phases*”, Rept. NOLTR 61-75 (AD 266607), U.S Naval Ordnance Laboratory, Aug 3, 1961.
- Buehler WJ, “*Intermetallic compound based materials for structural applications*”, *Proceedings of the Seventh navy Science symposium*, Rept. ONR-16, Vol 1, pp 1-30, 1963.
- Divinski SV, Stloukal I, Kral L, Herzig C, “*Diffusion of Titanium and Nickel in B2 NiTi*”, *Defect and Diffusion Forum Vols. 289-292*, pp 377-382, 2009.
- Duerig TW and Pelton AR, “*Ti-Ni Shape Memory Alloys*”, in *Materials Properties Handbook: Titanium Alloys*, Boyer R, Welsch G, and Collings EW, Ed., ASM International, p 1035-1048, 1994.
- Ekbom R, Haglund B-O, Hermansson L, “*Pulverteknik*” (swe text), Norstedts Tryckeri AB, Handbok 6, Utgåva 3, 1995.
- Eva, Software, Copyright Bruker-AXS, Chalmers University of Technology, License 2010/09. Data extracted May 2012.
- Firstov GS, Vitchev RG, Kumar H, Blanpain B, Van Humbeeck J, “*Surface oxidation of NiTi shape memory alloy*”, *Biomaterials* 23, 4863-4871, 2002.
- Frenzel J, George EP, Dlouhy A, Somsen C, Wagner MFX, Eggeler G, “*Influence of Ni on martensitic phase transformations in NiTi shape memory alloys*”, *Acta Materialia* 58, pp 3444-3458, 2010.
- German R, “*Powder Metallurgy of Iron and Steel*”, John Wiley & Sons, 1998.
- German R, “*Powder Metallurgy Science*”, 2nd ed., Metal Powder Industries Federation, pp 380-386, 1994.
- Gil FJ, Planell JA, “*Properties and clinical applications of shape memory alloys*”, *Biomaterials and bioengineering handbook*, Wise DL, 2000.
- Hara T, Ohba T, Otsuka K, Nishida M, “*Phase transformation and crystal structures of Ti<sub>2</sub>Ni<sub>3</sub> precipitates in Ti-Ni alloys*”, *Mater Trans JIM* 38, 277, 1997.
- Hoseney RC, “*Gelatinization phenomena of starch*”, *IFT Basic Symposium Series*, vol.13, pp 95-110, 1998.
- Ismail MH, Goodall R, Davies HA, Todd I, “*Porous NiTi alloy by metal injection moulding/sintering of elemental powders: Effect of sintering temperature*”, *Materials Letters*, 2011.

Koskimaki D, Marcinkowski MJ, Sastri AS, "Solid state diffusional transformations in the near-equiatomic Ni-Ti alloys", Trans. AIME, 1969.

Lyckfeldt O, Ferreira JMF, "Processing of porous ceramics by 'starch consolidation'", Journal of the European Ceramic Society, vol 18, pp.131-140, 1998.

Magalhães S<sup>1</sup>, Pavlícková M<sup>2</sup>, Nyborg L<sup>1</sup>, Lyckfeldt O<sup>3</sup>, Nordberg L-O<sup>4</sup>, "Optimisation of starch consolidation process for sintering of high speed steel powder compacts", <sup>1</sup>Chalmers University of Technology, Dept. of Materials science and engineering, Gothenburg, <sup>2</sup>The inst. Of chemical tech. in Prague, Dept. of metals and corr. Eng., <sup>3</sup>Swedish Ceramic Institute, Gothenburg, <sup>4</sup>Erasteel Kloster AB, R&D Laboratory, Söderfors, Sweden, 2003.

Miyazaki S, Ohmi Y, Otsuka K, Suzuki Y, "Characteristics of deformation and transformation pseudo-elasticity in TiNi alloys", J Phys 43, 1982.

Miyazaki S, Otsuka K, "Deformation and transition behavior associated with the R-phase in Ti-Ni alloys", Metall Trans 17A, 53, 1986.

Miyazaki S, Otsuka K, "Mechanical behaviour associated with the premartensitic rhombohedral-phase transition in a  $Ti_{50}Ni_{47}Fe_3$  alloy", Philos Mag A 50, 393, 1984.

Miyazaki S, Otsuka K, Suzuki Y, "Transformation pseudoelasticity and deformation behavior in a Ti-50.6 at%Ni alloy", Scripta Metall 15, 287, 1981.

Mueller MH and Knott HW, "The Crystal Structures of  $Ti_2Cu$ ,  $Ti_2Ni$ ,  $Ti_4Ni_2O$ , and  $Ti_4Cu_2O$ ", Trans. AIME, 1963.

Nishida M et al., "Precipitation processes in near-equiatomic TiNi shape memory alloys", Metall Trans, 1986.

Otsuka K & Wayman CM, "Shape Memory Materials", Cambridge University Press, Cambridge, 1998.

Otsuka K, Kakeshita T, "Elastic-Constant Behavior in Ti-Ni-Based Alloys", MRS Bulletin 27, 91, 2002.

Otsuka K, Shimizu K, "Pseudoelasticity and shape memory effects in alloys", Int Metals Rev 31, 93, 1986.

Otsuka K, Wayman CM, Nakai K, Sakamoto H, Shimizu K, "Superelasticity effects and stress-induced martensitic transformations in CuAlNi alloys", Acta Metall 207, 1976.

Ryhanen J, Kallioinen M, Tuukkanen J, Junila J, Niemela E, Sandvik P et al, "In vivo biocompatibility evaluation of nickel-titanium shape memory metal alloy: muscle and perineural tissue responses and capsule membrane thickness", J Biomed Mater Res 41, 481-8, 1998.

Saburi T, Nenno S, Fukuda T, "Crystal structure and morphology of the metastable X phase in shape memory titanium-nickel alloys", Journal of the Less-Common Metals 125, 157-66, 1986.

Saburi T, Nenno S, Fukuda TJ, "Crystal structure and morphology of the metastable X phase in shape memory Ti-Ni alloys", Less-Common Metals 125, 157, 1986.

Sanderow HI, “*Powder Metallurgy Methods and Design, Powder Metal Technologies and Applications*”, Vol 7, ASM Handbook, ASM International, pp 9-15, 1998.

Shaw JA, Kyriakides S, “*Thermomechanical aspects of NiTi*”, J. Mech. Phys. Solids, Vol 43, No. 8, pp 1243-1281, 1995.

Smallman RE, Ngan AHW, “*Physical metallurgy and advanced materials*”, Elsevier Ltd., pp 297-298, 2007.

Sonoda T, Watazu A, Kato K, Yamada T, Asahina T, “*Deposition of Ti/C compositional gradient film onto superplastic Ti-alloy by magnetron sputtering*”, Surf. Interface Anal., 36, pp 1141, 2004.

Taylor A, Floyd RW, “*Precision measurements of lattice parameters of non-cubic crystals*” Acta Crystall 3, 285, 1950.

Thierry B, Merhi Y, Bilodeau L, Trepanier C, Tabrizian M, “*Nitinol versus stainless steel stents: acute thrombogenicity study in an ex vivo porcine model*”, Biomaterials 23, 2997-3005, 2002.

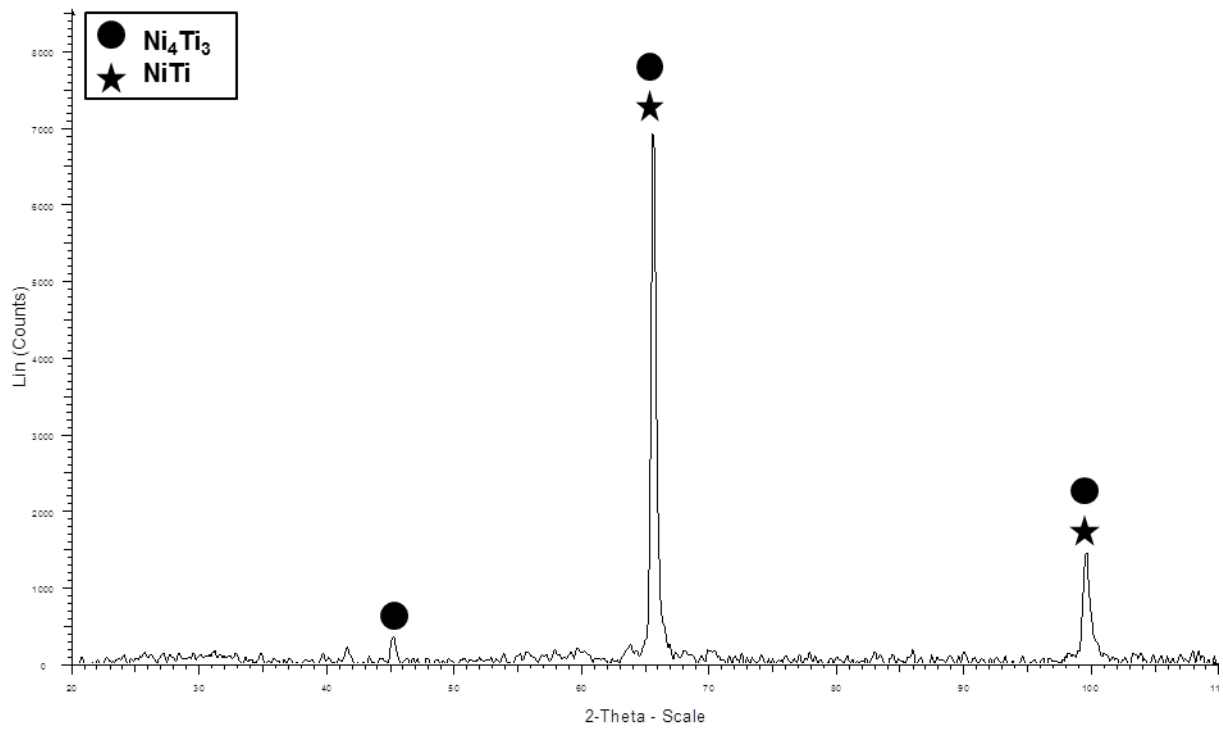
Wasilevski RJ, Butler SR, Hanlon JE, Worden D, “*Homogeneity range and the martensitic transformation in TiNi*”, Metall Trans, 1971.

Wayman CM, “*Shape Memory Alloys*”, MRS Bull, Vol 18, pp 49-56, 1993.

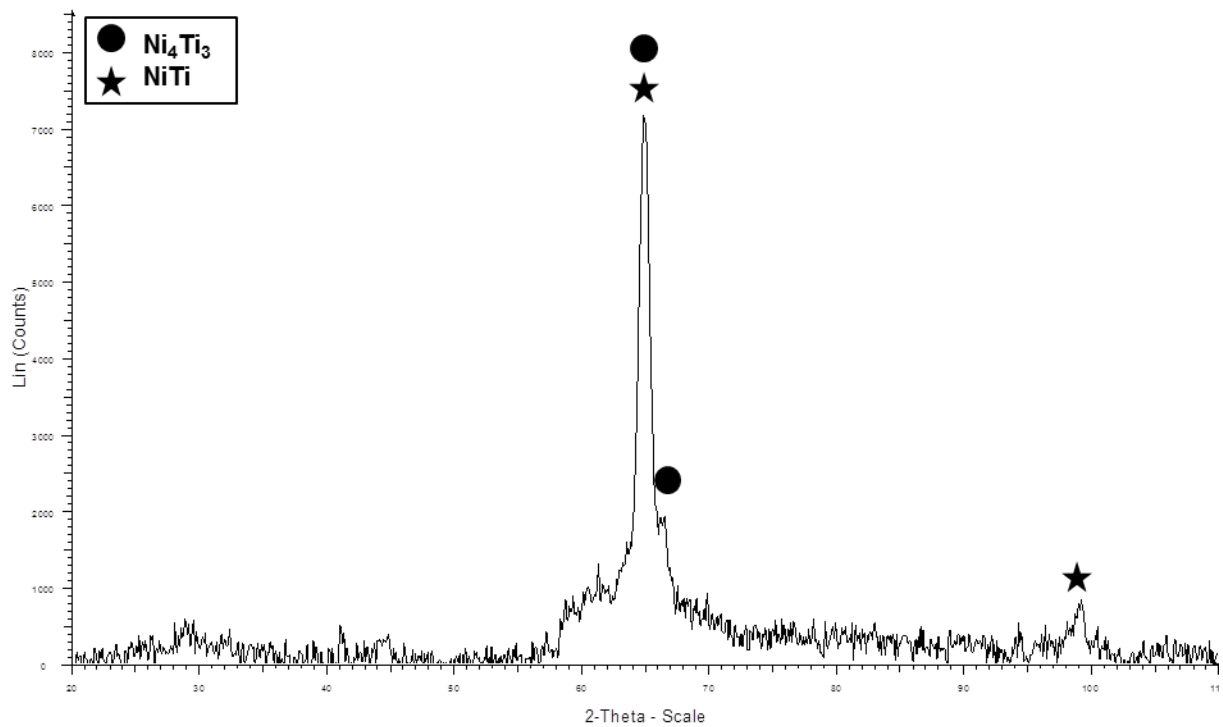
Yule AJ & Dunkley JJ, “*Atomization of Melts for Powder Production and Spray Deposition*”, Oxford University Press, 1994.



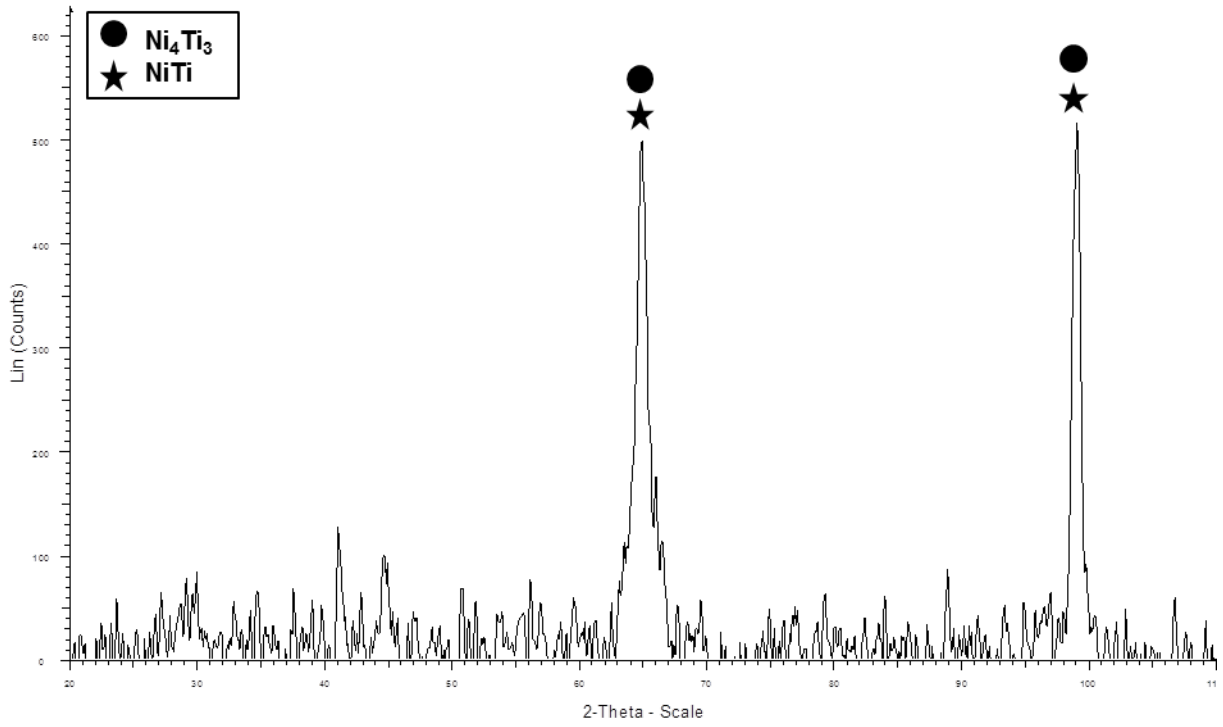
# APPENDIX



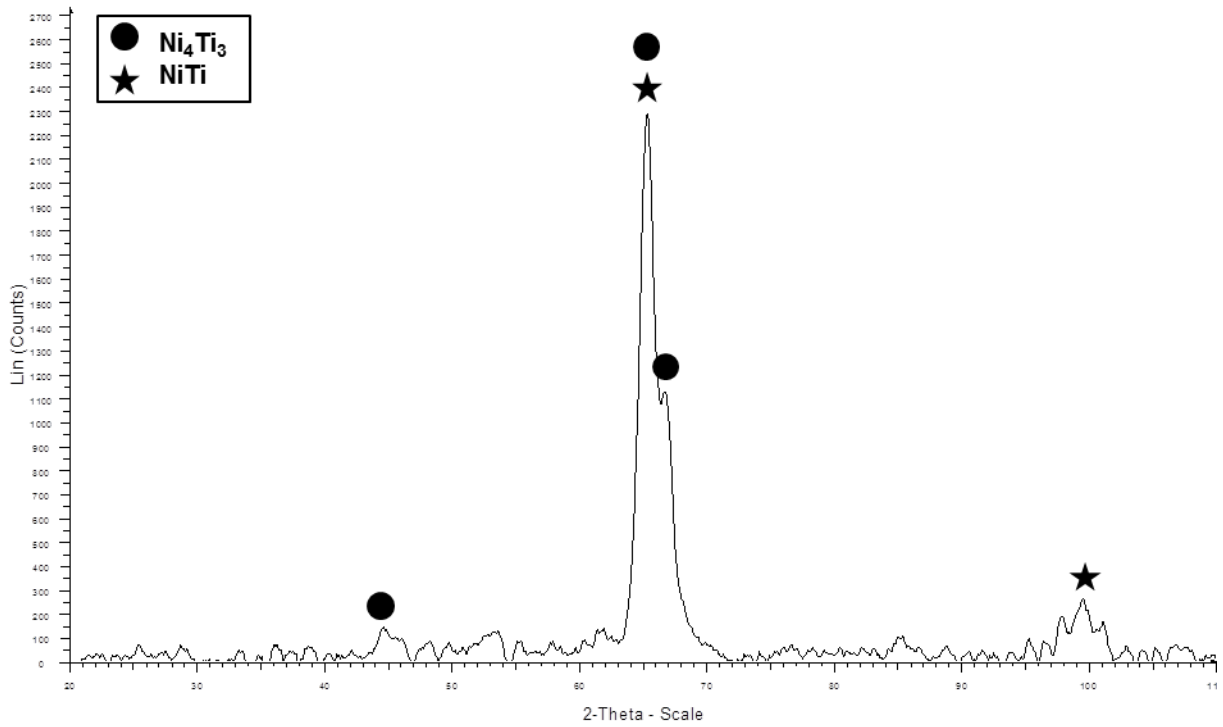
Appendix Figure 1: XRD scan of the powder, background removed.



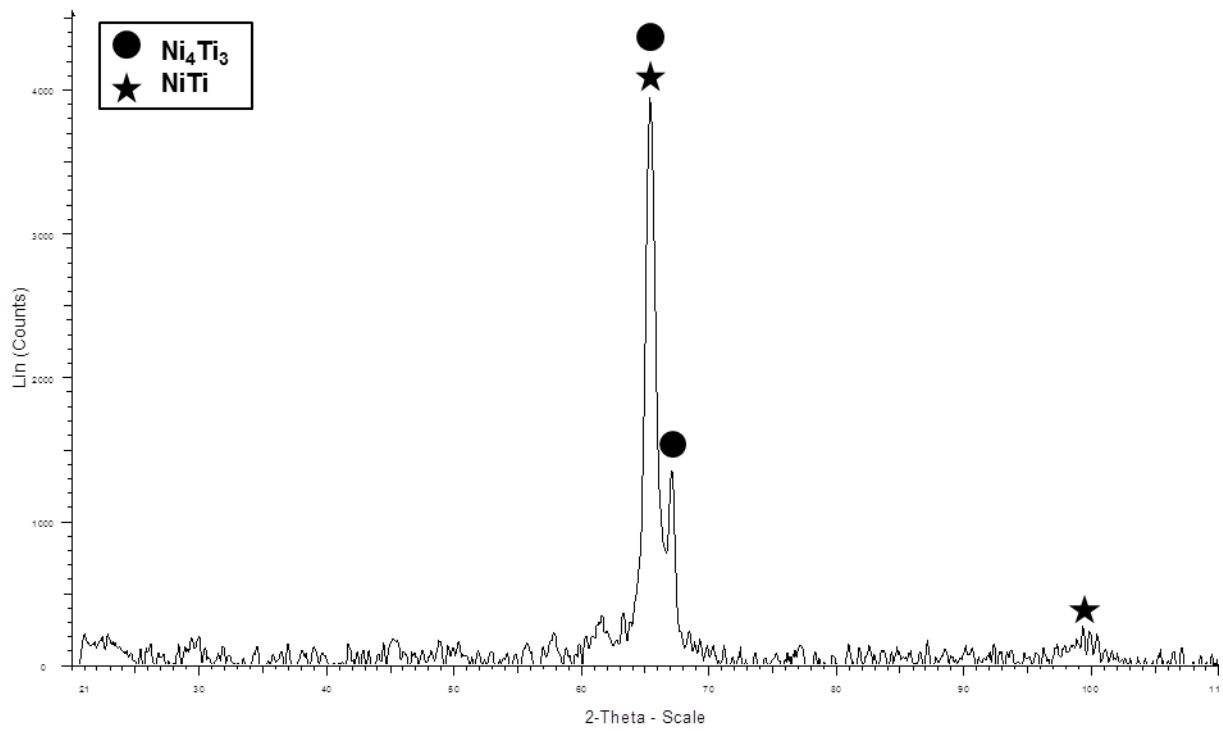
Appendix Figure 2: XRD scan of sample 2, dense volume, background removed.



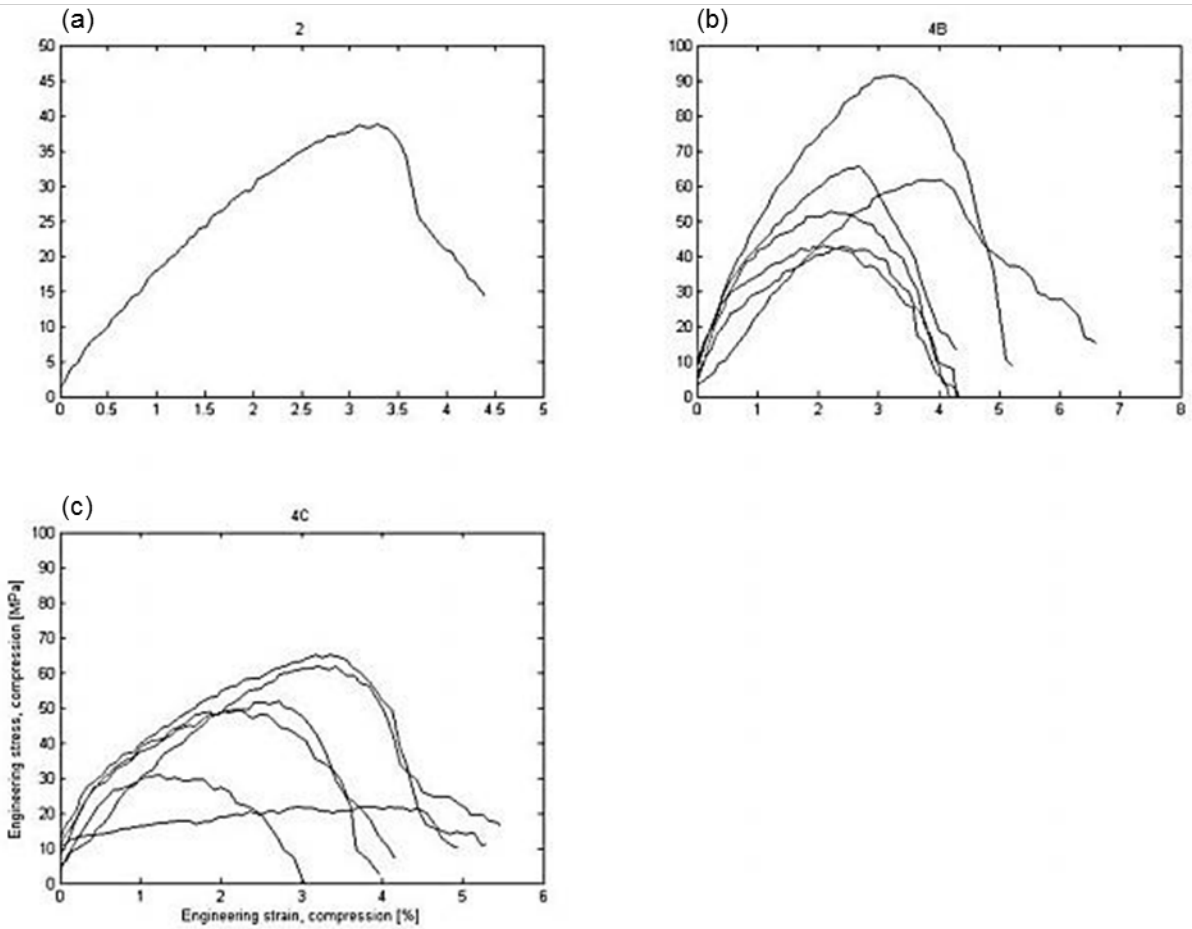
**Appendix Figure 3:** XRD scan of sample 2, porous volume, background removed.



**Appendix Figure 4:** XRD scan of sample 3A, background removed.



**Appendix Figure 5:** XRD scan of sample 4B, background removed.



**Appendix Figure 6:** Discarded engineering stress-strain ([MPa]-[%]) curves from the compression tests data of the as-sintered test pieces from test pieces of samples a) 2, b) 4B and c) 4C.

**Appendix Table 1:** Selection of PDF data for XRD of the actual setup (Eva, Software, 2010).

PDF no.	Phase	2 $\theta$ [°]	Intensity [%]*
00-018-0899	NiTi (B2)	66	100
		100	40
03-065-3957	Ni <sub>4</sub> Ti <sub>3</sub>	45	1.8
		65	100
		66	93
		100	25
01-072-0442	NiTi <sub>2</sub>	20	17
		59	29
		63	100
		70	26
		118	18
00-032-1383	TiC	55	80
		64	100
		97	60
01-086-2352	TiO	55	53
		64	100
		98	45
01-072-0443	Ni <sub>2</sub> Ti <sub>4</sub> O	59	31
		63	100
		70	28
		75	11
		118	20
*Intensity of maximum intensity			